


$B_s \rightarrow D_s^*$ form factors for the full q^2 range from lattice QCDJudd Harrison^{*,} and Christine T. H. Davies[†]

(HPQCD Collaboration)

SUPA, School of Physics and Astronomy, University of Glasgow, Glasgow, G12 8QQ, United Kingdom (Received 8 June 2021; accepted 28 April 2022; published 27 May 2022)

We compute the Standard Model semileptonic vector and axial-vector form factors for $B_s \rightarrow D_s^*$ decay across the full q^2 range using lattice QCD. We use the highly improved staggered quark (HISQ) action for all valence quarks, enabling us to normalize weak currents nonperturbatively. Working on second-generation MILC ensembles of gluon field configurations which include u , d , s , and c HISQ sea quarks and HISQ heavy quarks with masses from that of the c mass up to that of the b on the ensemble with the smallest lattice spacing, allows us to map out the heavy quark mass dependence of the form factors, and to constrain the associated discretization effects. We can then determine the physical form factors at the b mass. We use these to construct the differential and total rates for $\Gamma(B_s^0 \rightarrow D_s^{*-} \ell^+ \nu_\ell)$ and find $\Gamma_{\ell=e}/|\eta_{EW} V_{cb}|^2 = 2.07(17)_{\text{latt}}(2)_{\text{EM}} \times 10^{13} \text{ s}^{-1}$, $\Gamma_{\ell=\mu}/|\eta_{EW} V_{cb}|^2 = 2.06(16)_{\text{latt}}(2)_{\text{EM}} \times 10^{13} \text{ s}^{-1}$, and $\Gamma_{\ell=\tau}/|\eta_{EW} V_{cb}|^2 = 5.14(37)_{\text{latt}}(5)_{\text{EM}} \times 10^{12} \text{ s}^{-1}$, where η_{EW} contains the short-distance electroweak correction to G_F , the first uncertainty is from our lattice calculation, and the second allows for long-distance QED effects. The ratio $R(D_s^{*-}) \equiv \Gamma_{\ell=\tau}/\Gamma_{\ell=\mu} = 0.2490(60)_{\text{latt}}(35)_{\text{EM}}$. We also obtain a value for the ratio of decay rates $\Gamma_{\ell=\mu}(B_s \rightarrow D_s)/\Gamma_{\ell=\mu}(B_s \rightarrow D_s^*) = 0.443(40)_{\text{latt}}(4)_{\text{EM}}$, which agrees well with recent LHCb results. We can determine V_{cb} by combining our lattice results across the full kinematic range of the decay with experimental results from LHCb and obtain $|V_{cb}| = 42.2(1.5)_{\text{latt}}(1.7)_{\text{exp}}(0.4)_{\text{EM}} \times 10^{-3}$. A comparison of our lattice results for the shape of the differential decay rate to the binned, normalized differential decay rate from LHCb shows good agreement. We also test the impact of new physics couplings on angular observables and ratios which are sensitive to lepton flavor universality violation.

DOI: [10.1103/PhysRevD.105.094506](https://doi.org/10.1103/PhysRevD.105.094506)**I. INTRODUCTION**

The determination of the Cabibbo-Kobayashi-Maskawa (CKM) matrix elements requires precise theoretical calculations within the Standard Model (SM) and experimental measurements of quark flavor-changing decay processes. Meson semileptonic decay rates, to a meson in the final state, are parametrized by form factors that are related to matrix elements of the relevant quark flavor-changing weak current between the initial and final meson states. Lattice QCD has become the method of choice for the calculation of these matrix elements, and continuing efforts are being made to systematically improve the precision with which

form factors are known, in line with the projected reductions in experimental uncertainty.

Here we focus on semileptonic decays mediated by the quark-level weak transition $b \rightarrow c \ell^- \bar{\nu}_\ell$, which have seen many recent theoretical developments. The most precise determinations of the corresponding CKM matrix element, V_{cb} , make use of measurements of $B \rightarrow D^*$ and $B \rightarrow D$ [1] semileptonic decay, emphasizing the former due to favorable kinematic factors which do not suppress the differential decay rate as strongly near zero recoil. In these determinations, the experimental data for $B \rightarrow D^*$ are extrapolated using a parametrization scheme to zero recoil, where only a single form factor is needed, and matched to lattice calculations (e.g., Refs. [2,3]). Until recently, determinations of V_{cb} done in this way were in tension with the alternative inclusive determination, in which all charmed final-state mesons are considered, and it has since become apparent that the systematic uncertainties associated with the underlying model dependence of extrapolating to zero recoil were being underestimated, with more general parametrizations going some way in resolving the tension [4,5].

*judd.harrison@glasgow.ac.uk
†christine.davies@glasgow.ac.uk

Published by the American Physical Society under the terms of the [Creative Commons Attribution 4.0 International license](https://creativecommons.org/licenses/by/4.0/). Further distribution of this work must maintain attribution to the author(s) and the published article's title, journal citation, and DOI. Funded by SCOAP³.

It is clear, then, that an improved comparison between theory and experiment is needed, and that this must be done across the full physical kinematic range in order to remove any possible dependence upon the choice of parametrization scheme. Such a comparison requires an accurate calculation of the SM form factors using lattice QCD, which is made challenging by the presence of the light spectator quark accompanying the b and c quarks in the B and D^* meson states, respectively.

Recent work by LHCb [6] has also provided a complementary determination of $|V_{cb}|$ using the related $B_s \rightarrow D_s^{(*)}$ decay. While $B_s \rightarrow D_s^{(*)}$ decay has not been measured as precisely as $B \rightarrow D^{(*)}$, it is expected that the experimental uncertainty entering this determination will be decreased in future measurements. LHCb has also measured the shape of the normalized differential decay rate with respect to q^2 , the squared four-momentum transfer, for $B_s \rightarrow D_s^{(*)}$, allowing a direct comparison between theory and experiment.

Decays such as $B_s \rightarrow D_s^{(*)}$ and $B \rightarrow D^{(*)}$ involving a $b \rightarrow c \ell^- \bar{\nu}_\ell$ weak decay also allow us to probe lepton flavor universality. This may be done most straightforwardly by comparing the theoretical ratio in the SM of branching fractions for decays to a τ final-state lepton to those to a μ or e to the experimentally measured ratio. The corresponding ratio for $B \rightarrow D^{(*)}$, $R(D^{(*)})$, has been a source of tension with the SM for some time, e.g., Refs. [7,8], though recent measurements by Belle show consistency with the SM [9]. The sensitivity of other observables for $B \rightarrow D^{(*)}$ decay to lepton flavor universality violation (LFUV) has also recently been investigated [10]. The ratio for the related decay $B_c \rightarrow J/\psi \ell^- \bar{\nu}_\ell$, $R(J/\psi)$, has also recently been measured for the first time as part of the experimental program at LHCb [11]. Although this result currently has a large uncertainty, it is expected that this will be reduced significantly in future runs [12] to provide a further test of lepton flavor universality in that channel.

Pseudoscalar-to-pseudoscalar semileptonic decays, which are described in the SM by two form factors, have been more extensively studied using lattice QCD than pseudoscalar-to-vector semileptonic decays, which are described by four form factors in the SM. The $B \rightarrow D$ form factors were calculated away from zero recoil some time ago [13,14]. More recently, results for the $B \rightarrow D^*$ form factors away from zero recoil have become available [15]. The related $B_s \rightarrow D_s$ semileptonic form factors have recently been computed across the full physical q^2 range [16], while the relevant form factor for $B_s \rightarrow D_s^*$ has been computed only at zero recoil [3,17]. The form factors for $B_c \rightarrow J/\psi$ decay are less computationally expensive to calculate using lattice QCD than the form factors for $B \rightarrow D^*$ or $B_s \rightarrow D_s^*$, owing to the fact that all of the valence quarks are heavy. The J/ψ is also very narrow and far from

strong decay thresholds (unlike the D^*), making $B_c \rightarrow J/\psi$ decay an ideal starting point for lattice QCD calculations of pseudoscalar-to-vector form factors. The corresponding $B_c \rightarrow J/\psi$ form factors, computed in lattice QCD across the full q^2 range, recently became available [18], together with a high-precision theoretical value for the ratio $R(J/\psi)$ [19], together with other relevant LFUV-sensitive observables from Ref. [10].

A lattice QCD calculation of the $B_s \rightarrow D_s^*$ form factors is then well motivated: it will form an important stepping stone between the recent calculation of $B_c \rightarrow J/\psi$ form factors and a future lattice QCD calculation of the $B \rightarrow D^*$ form factors, as well as allowing for a complementary, model-independent determination of $|V_{cb}|$ when combined with LHCb results and a further channel to probe lepton flavor universality. $B_s \rightarrow D_s^*$ has an advantage over $B \rightarrow D^*$ from a lattice QCD perspective; there are no valence u/d quarks, and the D_s^* has no Zweig-allowed strong two-body decay mode, and so it has a very narrow width [20] that allows us to treat it as a stable meson.

Lattice QCD calculations involving a b quark have historically relied upon QCD discretizations which make use of the nonrelativistic nature of the b , or on the large mass of the b , to avoid the tradeoff between numerical expense and large discretization effects associated with placing a relativistic b quark on the lattice (e.g., Refs. [2,3]). Recently, however, it has become computationally viable to use lattices with sufficiently small lattice spacings to simulate relativistic heavy quarks with masses very close to the physical b mass [16–18].¹ These calculations carry with them the advantage that the same fully relativistic action is used for both b and c quarks, and so the current renormalization factors may be computed non-perturbatively and with a high precision. This is not typically possible for calculations using nonrelativistic actions where the current must instead be renormalized perturbatively, with the resulting truncation of the perturbation series contributing a potentially large systematic uncertainty (e.g., Ref. [3]).

In this paper, we apply the method of heavy-HISQ, which has seen much recent application in studies of the decays of b quarks (e.g., Refs. [16–18]), to the study of $B_s^0 \rightarrow D_s^{*-}(\rightarrow D_s^- \gamma) \ell^+ \nu_\ell$ decay across the full q^2 range.

The subsequent sections are arranged as follows:

- (1) In Sec. II, we give expressions for the differential decay rates, helicity amplitudes, and form factors relevant for $B_s^0 \rightarrow D_s^{*-} \ell^+ \nu_\ell$.
- (2) Section III gives the technical details of the lattice calculation.
- (3) In Sec. IV, we give the results for form factors from the lattice and discuss how to determine the form

¹This builds on the approach developed by HPQCD for heavy meson decay constants that has proved very successful [21–23].

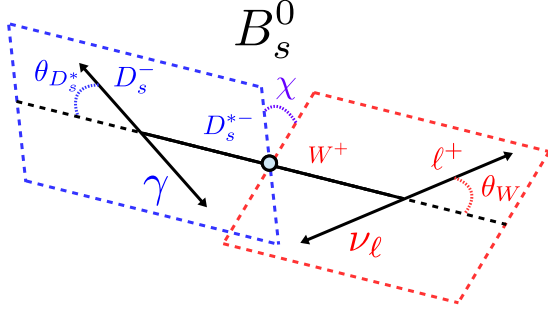


FIG. 1. Conventions for the angular variables entering the differential decay rate.

factors in the physical continuum limit. We also provide several tests of the stability of the analysis.

- (4) In Sec. V, we use the physical continuum form factors to make predictions for the differential decay rates for $B_S^0 \rightarrow D_S^{*-}(\rightarrow D_S^- \gamma) \ell^+ \nu_\ell$ and related quantities, as well as providing a breakdown of sources of uncertainty.
- (5) In Sec. VI, we compare our results to recent experimental results from LHCb for the shape of the differential rate and provide a determination of $|V_{cb}|$ using our results across the full kinematic range.
- (6) In Sec. VII, we investigate the effects of new physics couplings on lepton-flavor-universality-violating ratios.
- (7) Finally, in Sec. VIII, we summarize our findings.

II. THEORETICAL BACKGROUND

$B_S^0 \rightarrow D_S^{*-}(\rightarrow D_S^- \gamma) \ell^+ \nu_\ell$ decay has the same angular structure as the decay of $B_c^- \rightarrow J/\psi(\rightarrow \mu^+ \mu^-) \ell^- \bar{\nu}_\ell$ in the limit in which that the $\mu^+ \mu^-$ pair are massless, and hence are pure helicity states. The latter case was studied in Ref. [18]. We adopt the same angular definitions, given in Fig. 1, as for the $B_c \rightarrow J/\psi$ case. The differential rate is given by

$$\frac{d^4 \Gamma(B_S^0 \rightarrow D_S^{*-}(\rightarrow D_S^- \gamma) \ell^+ \nu_\ell)}{d \cos(\theta_{D_S^*}) d \cos(\theta_W) d\chi dq^2} = \mathcal{B}(D_S^* \rightarrow D_S \gamma) \mathcal{N} \sum_i k_i(\theta_W, \theta_{D_S^*}, \chi) \mathcal{H}_i(q^2), \quad (1)$$

where

$$\mathcal{N} = \frac{G_F^2}{(4\pi)^4} (1 + \delta_{EM}) |\eta_{EW}|^2 |V_{cb}|^2 \frac{3(q^2 - m_\ell^2)^2 |\vec{p}'|}{8M_{B_S}^2 q^2}. \quad (2)$$

Here, $|\vec{p}'|$ is the magnitude of the D_S^* spatial momentum in the B_S rest frame, and η_{EW} is a process-independent electroweak correction coming from box diagrams [24]. We include the factor $(1 + \delta_{EM})$, which we take as a

TABLE I. The helicity amplitude combinations and coefficients for them that appear in the differential rate [Eq. (1)]. Note that the k_i values for terms 1 and 2 have been swapped, as well as terms 4 and 5, compared to Ref. [19], since here we work with the conjugate mode $B_S^0 \rightarrow D_S^{*-}(\rightarrow D_S^- \gamma) \ell^+ \nu_\ell$.

i	\mathcal{H}_i	$k_i(\theta_W, \theta_{D_S^*}, \chi)$
1	$ H_+(q^2) ^2$	$\frac{1}{2} (1 + \cos(\theta_W))^2 (1 + \cos^2(\theta_{D_S^*}))$
2	$ H_-(q^2) ^2$	$\frac{1}{2} (1 - \cos(\theta_W))^2 (1 + \cos^2(\theta_{D_S^*}))$
3	$ H_0 ^2$	$2 \sin^2(\theta_W) \sin^2(\theta_{D_S^*})$
4	$\text{Re}(H_+ H_0^*)$	$-\sin(\theta_W) \sin(2\theta_{D_S^*}) \cos(\chi) (1 + \cos(\theta_W))$
5	$\text{Re}(H_- H_0^*)$	$\sin(\theta_W) \sin(2\theta_{D_S^*}) \cos(\chi) (1 - \cos(\theta_W))$
6	$\text{Re}(H_+ H_-^*)$	$\sin^2(\theta_W) \sin^2(\theta_{D_S^*}) \cos(2\chi)$
7	$\frac{m_\ell^2}{q^2} H_+(q^2) ^2$	$\frac{1}{2} (1 - \cos^2(\theta_W)) (1 + \cos^2(\theta_{D_S^*}))$
8	$\frac{m_\ell^2}{q^2} H_-(q^2) ^2$	$\frac{1}{2} (1 - \cos^2(\theta_W)) (1 + \cos^2(\theta_{D_S^*}))$
9	$\frac{m_\ell^2}{q^2} H_0 ^2$	$2 \cos^2(\theta_W) \sin^2(\theta_{D_S^*})$
10	$\frac{m_\ell^2}{q^2} H_t(q^2) ^2$	$2 \sin^2(\theta_{D_S^*})$
11	$\frac{m_\ell^2}{q^2} \text{Re}(H_+ H_0^*)$	$\sin(\theta_W) \sin(2\theta_{D_S^*}) \cos(\chi) \cos(\theta_W)$
12	$\frac{m_\ell^2}{q^2} \text{Re}(H_- H_0^*)$	$\sin(\theta_W) \sin(2\theta_{D_S^*}) \cos(\chi) \cos(\theta_W)$
13	$\frac{m_\ell^2}{q^2} \text{Re}(H_+ H_-^*)$	$-\sin^2(\theta_W) \sin^2(\theta_{D_S^*}) \cos(2\chi)$
14	$\frac{m_\ell^2}{q^2} \text{Re}(H_t H_0^*)$	$-4 \sin^2(\theta_{D_S^*}) \cos(\theta_W)$
15	$\frac{m_\ell^2}{q^2} \text{Re}(H_+ H_t^*)$	$-\sin(\theta_W) \sin(2\theta_{D_S^*}) \cos(\chi)$
16	$\frac{m_\ell^2}{q^2} \text{Re}(H_- H_t^*)$	$-\sin(\theta_W) \sin(2\theta_{D_S^*}) \cos(\chi)$

q^2 -independent uncertainty, to allow for the effects of QED long-distance radiation (we expect this to be dominated by final-state interactions between the electrically charged lepton and D_S^*). Following Ref. [25], we include this as a 1% uncertainty, which we take as the same for e and μ final states, but independent for the τ final state. Note that this choice is conservative, since in practice we expect there to be some amount of correlation between these effects for μ and τ final states, which we are neglecting here. We include this uncertainty separately in quoted results so that it may be adjusted in light of future calculations. The k_i and \mathcal{H}_i are given in Table I. Integrating over angles, the differential rate in q^2 is then given by

$$\frac{d\Gamma}{dq^2} = \mathcal{N} \times \frac{64\pi}{9} [(H_-^2 + H_0^2 + H_+^2) + \frac{m_\ell^2}{2q^2} (H_-^2 + H_0^2 + H_+^2 + 3H_t^2)]. \quad (3)$$

The helicity amplitudes are defined in terms of standard Lorentz-invariant form factors [26] as

TABLE II. Details of the gauge field configurations used in our calculation [27,28]. We use the Wilson flow parameter [31], w_0 , to fix the lattice spacing given in column 2. The physical value of w_0 was determined in Ref. [32] to be 0.1715(9) fm, and the values of w_0/a , which are used together with w_0 to compute a , were taken from Refs. [16,33,34]. Set 1 with $w_0/a = 1.9006(20)$ is referred to as “fine;” Set 2 with $w_0/a = 2.896(6)$ as “superfine;” Set 3 with $w_0/a = 3.892(12)$ as “ultrafine;” and Set 4 with $w_0/a = 1.9518(7)$ as “physical fine.” n_{cfg} and n_t give the number of configurations and the number of time sources, respectively. am_{l0} , am_{s0} , and am_{c0} are the masses of the sea up/down, strange, and charm quarks in lattice units. We also include the approximate mass of the Goldstone pion, computed in Ref. [22].

Set	a (fm)	$N_x \times N_t$	am_{l0}	am_{s0}	am_{c0}	M_π (MeV)	$n_{\text{cfg}} \times n_t$
1	0.0884	32×96	0.0074	0.037	0.440	316	980×16
2	0.0592	48×144	0.0048	0.024	0.286	329	489×4
3	0.0441	64×192	0.00316	0.0158	0.188	315	374×4
4	0.08787	64×96	0.0012	0.0363	0.432	129	300×8

$$\begin{aligned}
H_\pm(q^2) &= (M_{B_s} + M_{D_s^*})A_1(q^2) \mp \frac{2M_{B_s}|\vec{p}'|}{M_{B_s} + M_{D_s^*}}V(q^2), \\
H_0(q^2) &= \frac{1}{2M_{D_s^*}\sqrt{q^2}} \left(-4 \frac{M_{B_s}^2|\vec{p}'|^2}{M_{B_s} + M_{D_s^*}}A_2(q^2) \right. \\
&\quad \left. + (M_{B_s} + M_{D_s^*})(M_{B_s}^2 - M_{D_s^*}^2 - q^2)A_1(q^2) \right), \\
H_t(q^2) &= \frac{2M_{B_s}|\vec{p}'|}{\sqrt{q^2}}A_0(q^2), \tag{4}
\end{aligned}$$

and they correspond to the nonzero values of $\bar{e}_\mu^*(q, \lambda') \langle D_s^*(p', \lambda) | \bar{c} \gamma^\mu (1 - \gamma^5) b | B_s^0(p) \rangle$ for the different combinations of the D_s^* and W^- polarizations λ and λ' , respectively. The form factors in Eq. (4) are the standard Lorentz-invariant ones; their relations to the matrix elements are given by [26]

$$\begin{aligned}
&\langle D_s^*(p', \lambda) | \bar{c} \gamma^\mu b | B_s^0(p) \rangle \\
&= \frac{2iV(q^2)}{M_{B_s} + M_{D_s^*}} \epsilon^{\mu\nu\rho\sigma} \epsilon_\nu^*(p', \lambda) p'_\rho p_\sigma, \\
&\langle D_s^*(p', \lambda) | \bar{c} \gamma^\mu \gamma^5 b | B_s^0(p) \rangle \\
&= 2M_{D_s^*} A_0(q^2) \frac{\epsilon^*(p', \lambda) \cdot q}{q^2} q^\mu \\
&\quad + (M_{B_s} + M_{D_s^*}) A_1(q^2) \left[\epsilon^{*\mu}(p', \lambda) - \frac{\epsilon^*(p', \lambda) \cdot q}{q^2} q^\mu \right] \\
&\quad - A_2(q^2) \frac{\epsilon^*(p', \lambda) \cdot q}{M_{B_s} + M_{D_s^*}} \left[p^\mu + p'^\mu - \frac{M_{B_s}^2 - M_{D_s^*}^2}{q^2} q^\mu \right]. \tag{5}
\end{aligned}$$

We also have

$$\langle 0 | \bar{s} \gamma^\nu c | D_s^*(p', \lambda) \rangle = N_{D_s^*} \epsilon^\nu(p', \lambda), \tag{6}$$

$$\langle B_s^0(p) | \bar{b} \gamma^5 c | 0 \rangle = N_{B_s}, \tag{7}$$

and

$$\sum_\lambda \epsilon_\nu(p', \lambda) \epsilon_\mu^*(p', \lambda) = -g_{\nu\mu} + \frac{p'_\nu p'_\mu}{M^2}, \tag{8}$$

where $N_{D_s^*}$ and N_{B_s} are amplitudes proportional to the decay constant of the corresponding meson and ϵ is the D_s^* polarization vector. We use these when we come to extract the form factors in Eq. (5) from our lattice correlation functions.

III. LATTICE CALCULATION

As with previous heavy-HISQ calculations of semi-leptonic form factors involving $b \rightarrow c$ transitions—e.g., Refs. [16,18]—we work with the heavy meson at rest and give momentum to the charm quark. We use a range of heavy quark masses m_h between the charm and physical bottom quark mass, on ensembles with a range of lattice spacings between 0.09 fm and 0.045 fm. We use the second-generation $N_f = 2 + 1 + 1$ MILC ensembles which include light, strange, and charm HISQ sea quarks [27,28]. The details of these ensembles, together with the number of configurations we use, are given in Table II. On the ensemble with $a \approx 0.045$ fm, we are able to reach very near to the physical b mass. The heavy quark masses we use, together with the charm and strange quark valence masses, are given in Table III. Note that in this section, for notational simplicity, we consider the matrix elements in terms of continuum current operators. The nonperturbative renormalization of our lattice current operators is discussed in Sec. III C, where we use the values computed in Refs. [16,17]. We calculate, for general choices of current

TABLE III. Details of the strange, charm, and heavy valence masses.

Set	am_h^{val}	am_c^{val}	am_s^{val}
1	0.65, 0.725, 0.8	0.449	0.0376
2	0.427, 0.525, 0.65, 0.8	0.274	0.0234
3	0.5, 0.65, 0.8	0.194	0.0165
4	0.5, 0.65, 0.8	0.433	0.036

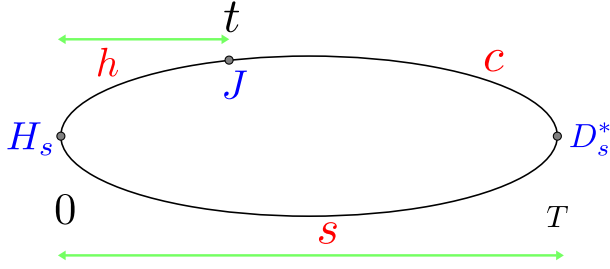


FIG. 2. Arrangement of propagators in the three-point function; we refer to c as the “active” charm quark, h as the “extended” heavy quark, and s as the “spectator” strange quark. J represents the insertion of either a vector or axial-vector current, and H_s and D_s^* represent the insertion of the corresponding meson interpolating operators.

operator $J = \bar{c}\Gamma h$ and D_s^* interpolating operator $\bar{c}\gamma^\nu s$, the correlation functions

$$\begin{aligned} C_{2\text{pt}}^{D_s^*}(t, 0) &= \langle 0 | \bar{s}\gamma^\nu c(t) (\bar{s}\gamma^\nu c(0))^\dagger | 0 \rangle, \\ C_{2\text{pt}}^{H_s}(t, 0) &= \langle 0 | (\bar{h}\gamma^5 s(t))^\dagger \bar{h}\gamma^5 s(0) | 0 \rangle, \\ C_{3\text{pt}}(T, t, 0) &= \langle 0 | \bar{s}\gamma^\nu c(T) \bar{c}\Gamma h(t) \bar{h}\gamma^5 s(0) | 0 \rangle. \end{aligned} \quad (9)$$

In order to improve statistics, we work with a random wall source placed at multiple origin times T_0 . From each of these sources we compute charm propagators with momenta inserted using twisted boundary conditions [29,30], as well as zero-momentum strange propagators and zero-momentum heavy quark propagators. Correlation functions with different T_0 's on a single configuration are binned. We tie the strange and charm propagators together (with the appropriate operators and conjugation) at time $T_0 + t$ to construct $C_{2\text{pt}}^{D_s^*}(t, 0)$, and we tie the strange and heavy propagators together at time $T_0 + t$ to construct $C_{2\text{pt}}^{H_s}(t, 0)$. To construct the three-point correlation functions, we use the strange propagator at time $T_0 - T$ as a source for the heavy quark propagator, which we tie together with the charm quark at time $T_0 + t - T$. The arrangement of propagators in $C_{3\text{pt}}$ is shown in Fig. 2, shifted so that the H_s operator is at time 0. We use twisted boundary conditions in the (1,1,0) direction with the twist chosen such that for the largest value of am_h on a given lattice the points span the physical q^2

TABLE IV. Values of twists, θ , in units of π/L_x , together with values of T used in the three-point functions in Eq. (9).

Set	θ	T
1	0, 0.3656, 0.7312, 1.097, 1.462, 1.828	14, 17, 20
2	0, 0.8019, 1.604, 2.406, 3.208, 4.009	22, 25, 28
3	0, 1.193, 2.387, 3.580, 4.773, 5.967	31, 36, 41
4	0, 0.7268, 1.454, 2.180, 2.907, 3.634	14, 17, 20

range evenly, where we estimate the maximum value of q^2 using the measured values of M_{H_s} from Ref. [16]. The twists we use are given in Table IV, in units of π/L_x , together with the values of T used in the three-point functions in Eq. (9).

The correlation functions in Eq. (9) are fit to the forms derived by considering the insertion of complete sets of states:

$$\begin{aligned} C_{2\text{pt}}^{D_s^*}(t, 0) &= \sum_n ((A^n)^2 e^{-tE^n} + (-1)^t (A_o^n)^2 e^{-tE_o^n}), \\ C_{2\text{pt}}^{H_s}(t, 0) &= \sum_n ((B^n)^2 e^{-tM^n} + (-1)^t (B_o^n)^2 e^{-tM_o^n}), \end{aligned} \quad (10)$$

and

$$\begin{aligned} C_{3\text{pt}}(T, t, 0) &= \sum_{n,m} (A^n B^m J^{nm} e^{-(T-t)E^n - tM^m} \\ &\quad + (-1)^{T+t} A_o^n B_o^m J_{oe}^{nm} e^{-(T-t)E_o^n - tM_o^m} \\ &\quad + (-1)^t A^n B_o^m J_{eo}^{nm} e^{-(T-t)E^n - tM_o^m} \\ &\quad + (-1)^T A_o^n B_o^m J_{oo}^{nm} e^{-(T-t)E_o^n - tM_o^m}). \end{aligned} \quad (11)$$

Here, n and m are integers corresponding to on-shell particle states of increasing energies, A^n and B^m are the amplitudes (together with relativistic normalization factors) of the D_s^* and H_s operators, respectively, and E_n and M_n are their energies and masses. The time-oscillating terms are a consequence of the use of staggered quarks, and the amplitudes and energies with an o subscript denote those quantities corresponding to time-doubled states. Note that for the matrix elements of J involving time-doubled states, we include an additional subscript e to make clear which of the D_s^* or H_s states is time-doubled. J^{nm} is then related to the matrix element of the current $\bar{c}\Gamma h(t)$ in Eq. (9) between the states labeled n and m . J_{eo}^{nm} then corresponds to the matrix element between the A^n state and the time-doubled B_o^m state, J_{oe}^{nm} to the matrix element between the time-doubled A_o^n state and B^m state, and J_{oo}^{nm} to the matrix element between the time-doubled A_o^n state and the time-doubled B_o^m state. The ground-state parameters are related to matrix elements as

$$\begin{aligned} A^0 &= \frac{N_{D_s^*}}{\sqrt{2E_{D_s^*}}} \left(1 + \frac{\vec{p}_\nu'^2}{M_{D_s^*}^2} \right)^{1/2}, \\ B^0 &= \frac{N_{H_s}}{\sqrt{2M_{H_s}}}, \end{aligned} \quad (12)$$

and

$$J_{(\nu,\Gamma)}^{00} = \sum_\lambda \frac{\epsilon^\nu(p', \lambda) \langle D_s^*(p', \lambda) | \bar{c}\Gamma b | H_s \rangle}{\lambda \sqrt{2E_{D_s^*} 2M_{H_s} (1 + \vec{p}_\nu'^2/M_{D_s^*}^2)}}, \quad (13)$$

where \vec{p}_ν' is the ν component of the D_s^* spatial momentum, with ν corresponding to the choice of polarization in Eq. (9),

TABLE V. Spin-taste operators used to isolate form factors. The first column is the operator used for the H_s , the second that for the D_s^* , and the third column is the operator used at the current.

	\mathcal{O}_{H_s}	$\mathcal{O}_{D_s^*}$	\mathcal{O}_J
V	$\gamma_0\gamma_5 \otimes \gamma_0\gamma_5$	$\gamma_1 \otimes \gamma_1\gamma_2$	$\gamma_3 \otimes \gamma_3$
A_0	$\gamma_5 \otimes \gamma_5$	$\gamma_1 \otimes 1$	$\gamma_5 \otimes \gamma_5$
A_1	$\gamma_5 \otimes \gamma_5$	$\gamma_3 \otimes \gamma_3$	$\gamma_3\gamma_5 \otimes \gamma_3\gamma_5$
A_2	$\gamma_5 \otimes \gamma_5$	$\gamma_1 \otimes \gamma_1$	$\gamma_1\gamma_5 \otimes \gamma_1\gamma_5$

with current $\bar{c}\Gamma h$. We also compute $\gamma_5 \otimes \gamma_5$ pseudoscalar η_h and η_c correlation functions, which we will use to parametrize the physical m_h dependence of our form factors as well as to determine the valence and sea charm quark mass mistunings. Note that for the η correlation functions we neglect disconnected contributions.

A. Extraction of form factors

The combinations of spin-taste operators we use here to access the form factors, and the methods used to extract the form factors from the matrix elements, are the same as in Ref. [18]. We repeat these methods below for reference. The combinations of spin-taste operators are given in Table V.

We give the D_s^* spatial momentum $\vec{p}' = (k, k, 0)$. In order to isolate all the form factors, we need one component of \vec{p}' to be zero. Keeping both of the others nonzero minimizes the discretization errors for a given magnitude of p' .

1. Extracting $V(q^2)$

Here we choose $\mu = 3$ and $\nu = 1$ and find

$$V(q^2) = \Phi(k) \frac{M_{H_s} + M_{D_s^*}}{2ikM_{H_s}} J_{(1,\gamma^3)}^{00}, \quad (14)$$

where we have defined the relativistic normalization

$$\Phi(k) = \sqrt{2E_{D_s^*} 2M_{H_s} (1 + k^2/M_{D_s^*}^2)} \quad (15)$$

with k the ν component of p' .

2. Extracting $A_0(q^2)$

In order to isolate $A_0(q^2)$, following Ref. [35], we make use of the partially conserved axial-vector current (PCAC) relation $\langle \partial A \rangle = (m_c + m_h) \langle P \rangle$, where $A = \bar{c}\gamma^5\gamma^\nu h$ and $P = \bar{c}\gamma^5 h$. From Eq. (5), we have

$$\begin{aligned} & \sum_{\lambda} \epsilon^\nu(p', \lambda) q_\mu \langle D_s^*(p', \lambda) | \bar{c}\gamma^\mu\gamma^5 h | H_s \rangle \\ &= \sum_{\lambda} \epsilon^\nu(p', \lambda) 2M_{D_s^*} A_0(q^2) \epsilon^*(p', \lambda) \cdot q \\ &= \frac{2kE_{D_s^*} M_{H_s}}{M_{D_s^*}} A_0(q^2). \end{aligned} \quad (16)$$

Taking $\Gamma = \gamma^5$ and $\nu = 1$ in Eq. (13) and multiplying by $m_c + m_b$, we then have

$$A_0(q^2) = \Phi(k) \frac{(m_c + m_b) M_{D_s^*}}{2kE_{D_s^*} M_{H_s}} J_{(1,\gamma^5)}^{00}. \quad (17)$$

3. Extracting $A_1(q^2)$

In order to isolate A_1 , we use the axial-vector current $\Gamma = \bar{c}\gamma^\mu\gamma^5 h$ and the D_s^* operator $\bar{s}\gamma^\nu c$ and choose $\mu = \nu = 3$ along the spatial direction with zero D_s^* momentum. Using Eq. (5), this gives

$$\begin{aligned} & \sum_{\lambda} \epsilon^3(p', \lambda) \langle D_s^*(p', \lambda) | \bar{c}\gamma^3\gamma^5 h | H_s \rangle \\ &= (M_{D_s^*} + M_{H_s}) A_1(q^2), \end{aligned} \quad (18)$$

which gives, in terms of J^{00} ,

$$A_1(q^2) = \Phi(0) \frac{J_{(3,\gamma^3\gamma^5)}^{00}}{M_{D_s^*} + M_{H_s}}. \quad (19)$$

4. Extracting $A_2(q^2)$

The extraction of A_2 is more complicated than the extraction of the other form factors, since no trivial choice of directions in axial-vector and D_s^* operators isolates the contribution of A_2 relative to A_1 or A_0 . We use axial-vector current operator $J = \bar{c}\gamma^1\gamma^5 h$ and D_s^* operator $\bar{s}\gamma^1 c$. This yields contributions from each form factor,

$$\begin{aligned} \Phi(k) J_{(1,\gamma^1\gamma^5)}^{00} &= \sum_{\lambda} \epsilon^1(p', \lambda) \langle D_s^*(p', \lambda) | \bar{c}\gamma^1\gamma^5 h | H_s \rangle \\ &= -\frac{2k^2 E_{D_s^*} M_{H_s}}{q^2 M_{D_s^*}} A_0(q^2) \\ &\quad + (M_{H_s} + M_{D_s^*}) \left(1 + \frac{k^2}{M_{D_s^*}^2} + \frac{E_{D_s^*} M_{H_s} k^2}{M_{D_s^*}^2 q^2} \right) A_1(q^2) \\ &\quad - A_2(q^2) \frac{k^2 E_{D_s^*} M_{H_s}}{M_{D_s^*}^2 (M_{H_s} + M_{D_s^*})} \left(1 + \frac{M_{H_s}^2 - M_{D_s^*}^2}{q^2} \right). \end{aligned} \quad (20)$$

We must then subtract the A_0 and A_1 contributions to obtain A_2 .

TABLE VI. Correlator fit priors. We take $\Delta E_i^{(o)} = \Lambda_{\text{QCD}} \times 1.0(0.75)$, where $\Delta E_i^{(o)} = E_{i+1}^{(o)} - E_i^{(o)}$, $i \geq 0$, and here for our correlator fits we take $\Lambda_{\text{QCD}} = 0.75$ GeV, $\Omega_{D_S^*} = (2.1^2 + p'^2)^{\frac{1}{2}}$, and $\Omega_{H_S} = M_{H_S}^{\text{max}}(am_h/0.8)^{\frac{1}{2}}$, where $M_{H_S}^{\text{max}}$ is the value of M_{H_S} corresponding to the largest am_h , taken from Ref. [17]. While $\Omega_{D_S^*}$ was chosen to follow the relativistic dispersion relation, Ω_{H_S} was chosen heuristically to give prior values approximately following the observed H_S masses on each set while remaining suitably loose so as not to constrain the fit results.

Prior	η_h	η_c	$D_S^*(p')$	H_S
E_0/GeV	$m_h \times 2.5(0.5)$	3.0(0.9)	$\Omega_{D_S^*} 1.0(0.3)$	$\Omega_{H_S} 1.0(0.3)$
E_0^o/GeV	$\Omega_{D_S^*} 1.2(0.5)$	$\Omega_{H_S} 1.2(0.5)$
$A(B)_{(o)}^n$	0.1(5.0)	0.1(5.0)	0.1(5.0)	0.1(5.0)

B. Fit parameters

The correlator fits to Eq. (10) and Eq. (11) were done using the *corrfit* PYTHON package [36]. These were done simultaneously for all correlation functions on each ensemble, taking all correlations into account. For ground-state priors we take $E_0^{D_S^*} = 2.1(0.6)$ GeV and $M_0^{H_S} = M_{\text{max}}^{H_S}(am_h/0.8)^{1/2} \times 1(0.3)$ GeV, where $M_{\text{max}}^{H_S}$ is the value of M_{H_S} from Ref. [16] corresponding to the largest value of am_h . The m_h dependence of the prior for $M_0^{H_S}$ was chosen heuristically to give prior values approximately following the observed H_S masses on each set while remaining suitably loose so as not to constrain the fit results. Our priors for the η_c, η_h , and lowest oscillating state energies, as well as amplitudes, are given in Table VI, while for the matrix elements of J we take priors 0(1).

In order to reduce excited state contamination and to improve the stability and convergence of the fits, we

exclude data for $t < t_{\text{min}}$ and for $t > t_{\text{max}}$. We also specify an SVD cut using the tools available in Ref. [36]. We use several different choices of $t_{\text{min}}, t_{\text{max}}$, and SVD cut, and we investigate the stability of our subsequent analysis with respect to taking different combinations of fit parameters. These fit parameters are given in Table VII, and the stability of our analysis will be discussed later in Sec. IV.

C. Nonperturbative current renormalization

The renormalization factors relating the HISQ lattice currents in Table V to the continuum currents considered in Sec. II are the same as those used in Ref. [18]. These were computed previously in Ref. [16] for the local vector current and in Ref. [17] for the axial current, using the partially conserved vector current (PCVC) and axial-vector current (PCAC) relations respectively. As in the previous $B_c \rightarrow J/\psi$ form factor calculation, we include some values of the heavy quark masses for which the Z factors were not computed. We interpolate between the values computed in Refs. [16,17] on Sets 1 and 4 for masses $am_h = 0.725$ and $am_h = 0.65$, respectively, setting the uncertainties of the interpolated factors equal to the largest uncertainty of the other values. We tabulate these renormalization factors in Table VIII, where we include the am -dependent discretization correction terms, Z^{disc} , for the HISQ-quark tree-level wave function renormalization computed in Ref. [37]. These receive contributions beginning at $\mathcal{O}((am_h)^4)$ for HISQ and as such are close to 1. The total renormalization factor for an (axial-)vector current is then given by $Z^{V(A)}Z^{\text{disc}}$. Note, however, that no renormalization factor is required for A_0 , since we determine it using the absolutely normalized $\gamma_5 \otimes \gamma_5$ pseudoscalar current together with the PCAC relation.

We neglect correlations between the renormalization factors Z and our lattice data, since the Z factors have uncertainties which are typically at least an order of magnitude smaller than the corresponding form factors.

IV. RESULTS

Here we give the lattice results for the form factors, which were extracted from the matrix elements in Eq. (13) resulting from the fits discussed in Sec. III. For V, A_1 , and

TABLE VII. Details of fit parameters, together with variations used in Sec. IV C to check stability. ΔT indicates the number of data points at the extremities of correlation functions not included in the fit. Bold values are those used to produce our final results. $\chi^2/\text{d.o.f.}$ is estimated by introducing SVD and prior noise as in Ref. [36]. We do not compute χ^2 values including prior and SVD noise for those fits with $n_{\text{exp}} = 4$.

Set	n_{exp}	$\Delta T_{3\text{pt}}$	$\Delta T_{2\text{pt}}^{D_S^*}$	$\Delta T_{2\text{pt}}^{H_S}$	SVD cut	$\chi^2/\text{d.o.f.}$	δ
1	3	2	4	4	0.005	1.06	0
	3	2	4	4	0.01	1.09	1
	3	3	6	6	0.005	0.96	2
	4	2	4	4	0.005	...	3
2	3	2	4	4	0.025	1.04	0
	3	2	4	4	0.05	1.00	1
	3	3	7	7	0.025	0.98	2
	4	2	4	4	0.025	...	3
3	3	3	6	6	0.005	1.02	0
	3	3	6	6	0.01	1.01	1
	3	4	8	8	0.005	0.99	2
	4	3	6	6	0.005	...	3
4	3	2	5	5	0.01	1.03	0
	3	2	5	5	0.025	1.04	1
	3	3	7	7	0.01	1.05	2
	4	2	5	5	0.01	...	3

TABLE VIII. Z factors from Refs. [16,17] for the axial-vector and vector operators used in this work, together with the discretization corrections. Z^A and Z^V values for $am_h = 0.725$ on Set 1 and $am_h = 0.65$ on Set 4 were obtained by interpolation from the other values for those sets. The uncertainties of the interpolated factors are set equal to the largest uncertainty of the other values.

Set	am_h	Z^A	Z^V	Z^{disc}
1	0.65	1.03740(58)	1.0254(35)	0.99635
	0.725	1.04030(58)	1.0309(35)	0.99491
	0.8	1.04367(56)	1.0372(32)	0.99306
2	0.427	1.0141(12)	1.0025(31)	0.99931
	0.525	1.0172(12)	1.0059(33)	0.99859
	0.65	1.0214(12)	1.0116(37)	0.99697
	0.8	1.0275(12)	1.0204(46)	0.99367
3	0.5	1.00896(44)	1.0029(38)	0.99889
	0.65	1.01363(49)	1.0081(43)	0.99704
	0.8	1.01968(55)	1.0150(49)	0.99375
4	0.5	1.03184(47)	1.0134(24)	0.99829
	0.65	1.03717(47)	1.0229(29)	0.99645
	0.8	1.04390(39)	1.0348(29)	0.99315

A_2 , these include the renormalization factors given in Table VIII. The values of the form factors are tabulated in the Appendix A in Tables XVIII, XIX, XX, and XXI together with the value of the momentum component in lattice units, ak , of the D_s^* in the x and y directions.

Our results for the D_s^* and η_c masses on each set are given in lattice units in Table IX together with the corresponding spin-taste operators. Our results for the H_s and η_h masses are given in lattice units in Table X together with the corresponding spin-taste operators.

We fit the heavy mass and lattice spacing dependence of our lattice form factor results in order to determine the physical continuum form factors, following the method in Ref. [18]. We repeat the details of this fit here, as well as performing similar tests of stability.

A. Extrapolation to the physical point

We parametrize the q^2 dependence using the z expansion [38–40]. We first change variables from q^2 to $z(q^2, t_0)$, with

TABLE IX. Results for the D_s^* masses for the local spin-taste operator $\gamma_1 \otimes \gamma_1$ and 1-link operators $\gamma_1 \otimes 1$ and $\gamma_1 \otimes \gamma_1 \gamma_2$ used in our calculation; see Table V. Here we also include values for the local $\gamma_5 \otimes \gamma_5 \eta_c$ mass.

Set	$aM_{D_s^*}$			aM_{η_c}
	$\gamma_1 \otimes \gamma_1$	$\gamma_1 \otimes 1$	$\gamma_1 \otimes \gamma_1 \gamma_2$	$\gamma_5 \otimes \gamma_5$
1	0.96451(48)	0.96493(56)	0.96422(67)	1.364940(48)
2	0.63482(80)	0.6350(12)	0.6347(12)	0.896802(67)
3	0.47327(58)	0.47284(99)	0.4727(11)	0.66721(12)
4	0.93975(48)	0.93957(63)	0.93928(68)	1.329310(45)

TABLE X. Results for the η_h masses and H_s masses for the local spin-taste operators $\gamma_5 \otimes \gamma_5$ and $\gamma_0 \gamma_5 \otimes \gamma_0 \gamma_5$ that we use in our calculation; see Table V.

Set	am_h	$aM_{H_s}(\gamma_5 \otimes \gamma_5)$	$aM_{H_s}(\gamma_0 \gamma_5 \otimes \gamma_0 \gamma_5)$	aM_{η_h}
1	0.65	1.12498(16)	1.12550(27)	1.775201(42)
	0.725	1.20419(17)	1.20467(30)	1.921510(40)
	0.8	1.28122(19)	1.28166(33)	2.064184(39)
2	0.427	0.77431(28)	0.77456(59)	1.233625(58)
	0.525	0.88460(35)	0.88496(73)	1.439573(54)
	0.65	1.01969(45)	1.02019(92)	1.693959(49)
	0.8	1.17464(56)	1.1752(12)	1.987607(46)
3	0.5	0.80339(34)	0.8020(12)	1.343315(81)
	0.65	0.96484(40)	0.9634(14)	1.650857(69)
	0.8	1.11894(45)	1.1174(15)	1.946422(60)
4	0.5	0.95452(14)	0.95487(26)	1.470108(45)
	0.65	1.11976(19)	1.11987(34)	1.773763(42)
	0.8	1.27577(25)	1.27571(44)	2.062919(42)

$$z(q^2, t_0) = \frac{\sqrt{t_+ - q^2} - \sqrt{t_+ - t_0}}{\sqrt{t_+ - q^2} + \sqrt{t_+ - t_0}}. \quad (21)$$

We take t_0 equal to the maximum physical value of q^2 ,

$$t_0 = (M_{H_s} - M_{D_s^*})^2, \quad (22)$$

and

$$t_+ = (M_H + M_{D^*})^2. \quad (23)$$

Since we do not have direct access to M_H , the mass of the $h\bar{u}$ pseudoscalar meson, we instead use $M_H^{\text{latt}} = M_{H_s} - (M_{B_s^{\text{phys}}} - M_B^{\text{phys}})$. We use the physical value of M_{D^*} from experiment, since our valence charm masses are tuned to the physical value, and the light quark mass mistuning is accounted for elsewhere in the fit function. The numerical values of the physical B , B_s , and D^* masses are given in Table XI. The form factors include poles resulting from $b\bar{c}$ states, with masses below the pair production threshold t_+ , with the same quantum numbers as the corresponding current. We include these poles, which are the same for $B_s \rightarrow D_s^*$ as for $B_c \rightarrow J/\psi$ and $B \rightarrow D^*$, using the same form as in Ref. [18], which was taken from Refs. [38,40]:

$$P(q^2) = \prod_{M_{\text{pole}}} z(q^2, M_{\text{pole}}^2). \quad (24)$$

We approximate the heavy mass dependence of the pole masses using $M_{\text{pole}} = M_{H_s} + M_{B_s^{\text{phys}}} - M_{B_s^{\text{phys}}}$, which ensures that in the physical continuum limit the correct physical pole masses are recovered. The physical pole masses used here are listed in Table XII.

Our fit function then takes the form

$$F(q^2) = \frac{1}{P(q^2)} \sum_{n=0}^3 a_n z^n \mathcal{N}_n, \quad (25)$$

TABLE XI. Values used in our fits for the physical masses of relevant mesons, in GeV. These are from the Particle Data Group [41] except for the unphysical η_s , which we take from lattice calculations of the mass of the pion and kaon [42]. The η_s and η_c masses are used to set mass mistuning terms in our fit and so include an uncertainty. The other masses are used as kinematic parameters in setting up our fit in z space and are used without uncertainties. In light of the results of Ref. [43], we have checked that using a value of $M_{\eta_c}^{\text{phys}}$ 10 MeV lower than that given here, allowing for the effects of QED and $c\bar{c}$ annihilation, has only a very small effect on our results at the level of 0.05σ .

Meson	M^{phys} [GeV]
η_b	9.3889
B_s	5.3669
B	5.27964
η_c	2.9863(27)
D_s^*	2.112
D^*	2.010
η_s	0.6885(22)

TABLE XII. Expected B_c pseudoscalar, vector, and axial-vector masses below the BD^* threshold that we use in our pole factor, Eq. (24). Pseudoscalar values for the ground state and first radial excitation are taken from experiment [41,44–46]; the other values are taken from Ref. [3] and are derived from lattice QCD calculations [47] and model estimates [48–50].

0^- /GeV	1^- /GeV	1^+ /GeV
6.275	6.335	6.745
6.872	6.926	6.75
7.25	7.02	7.15
	7.28	7.15

where $P(q^2)$ is the appropriate pole form for that form factor [constructed using 1^- states for $V(q^2)$, 1^+ states for $A_1(q^2)$ and $A_2(q^2)$, or 0^- states for $A_0(q^2)$] as in Eq. (24). The remainder of the fit function is a polynomial in z with separate coefficients, a_n , for each form factor that take the form

$$a_n = \sum_{j,k,l=0}^3 b_n^{jkl} \Delta_h^{(j)} \left(\frac{am_c^{\text{val}}}{\pi}\right)^{2k} \left(\frac{am_h^{\text{val}}}{\pi}\right)^{2l}. \quad (26)$$

The $\Delta_h^{(j)}$'s allow for the dependence on the heavy quark mass using the η_h mass as a physical proxy for this. We have $\Delta_h^{(0)} = 1$ and

$$\Delta_h^{(j \neq 0)} = \left(\frac{2\Lambda}{M_{\eta_h}}\right)^j - \left(\frac{2\Lambda}{M_{\eta_b}^{\text{phys}}}\right)^j. \quad (27)$$

The physical value of the η_b mass is given in Table XI, and we take $\Lambda = 0.5$ GeV. The remainder of Eq. (25), \mathcal{N}_n ,

takes into account the effect of mistuning the valence and sea quark masses for each form factor, where

$$\mathcal{N}_n = 1 + A_n \delta_{m_c}^{\text{val}} + B_n \delta_{m_c}^{\text{sea}} + C_n \delta_{m_s}^{\text{val}} + D_n \delta_{m_s}^{\text{sea}} + E_n \delta_{m_l}^{\text{sea}}, \quad (28)$$

with

$$\begin{aligned} \delta_{m_c}^{\text{val}} &= (am_c^{\text{val}} - am_c^{\text{tuned}})/am_c^{\text{tuned}}, \\ \delta_{m_c}^{\text{sea}} &= (am_c^{\text{sea}} - am_c^{\text{tuned}})/am_c^{\text{tuned}}, \\ \delta_{m_s}^{\text{val}} &= (am_s^{\text{val}} - am_s^{\text{tuned}})/(10am_s^{\text{tuned}}), \\ \delta_{m_{s(l)}}^{\text{sea}} &= (am_{s(l)}^{\text{sea}} - am_{s(l)}^{\text{tuned}})/(10am_s^{\text{tuned}}). \end{aligned} \quad (29)$$

Using a ratio of lattice quark masses to $10am_s^{\text{tuned}}$ is a convenient proxy for the usual chiral expansion parameter, which is a ratio of squared meson masses to Λ_χ^2 where $\Lambda_\chi = 4\pi f_\pi$. The tuned values of the quark masses are given by

$$am_c^{\text{tuned}} = am_c^{\text{val}} \frac{M_{\eta_c}^{\text{phys}}}{M_{\eta_c}} \quad (30)$$

and

$$am_s^{\text{tuned}} = am_s^{\text{val}} \left(\frac{M_{\eta_s}^{\text{phys}}}{M_{\eta_s}}\right)^2. \quad (31)$$

M_{η_c} on each set is given in lattice units in Table IX, and we use the values of M_{η_s} given in Ref. [17], which used the same values of am_s^{val} . To determine the mistuning of the $u/d = l$ quark mass in the sea, we take

$$am_l^{\text{tuned}} = am_s^{\text{tuned}}/[m_s/m_l]^{\text{phys}}, \quad (32)$$

with $[m_s/m_l]^{\text{phys}} = 27.18(10)$ from Ref. [22]. We take priors of 0(1) for each b_n , multiplying terms of order $\mathcal{O}(a^2)$ by 0.5 in line with the tree-level a^2 improvement of the HISQ action [51]. We also use priors of 0.0(0.1) for B_n , motivated by the results of the analysis of m_c^{sea} effects on w_0 in Ref. [34]. We take priors of 0.0(0.5) for D_n and E_n for each form factor, since sea quark mistuning effects enter at one loop. All of the remaining priors are taken as 0(1), motivated by the analysis done in Ref. [18] using the empirical Bayes criterion, which showed that for the $B_c \rightarrow J/\psi$ form factors this choice was conservative, which we expect to be the case here also. The physical masses used for the η_c and η_s are given in Table XI.

We impose the kinematical constraint

$$2M_{D_s^*} A_0(0) = (M_{D_s^*} + M_{H_s}) A_1(0) + (M_{D_s^*} - M_{H_s}) A_2(0). \quad (33)$$

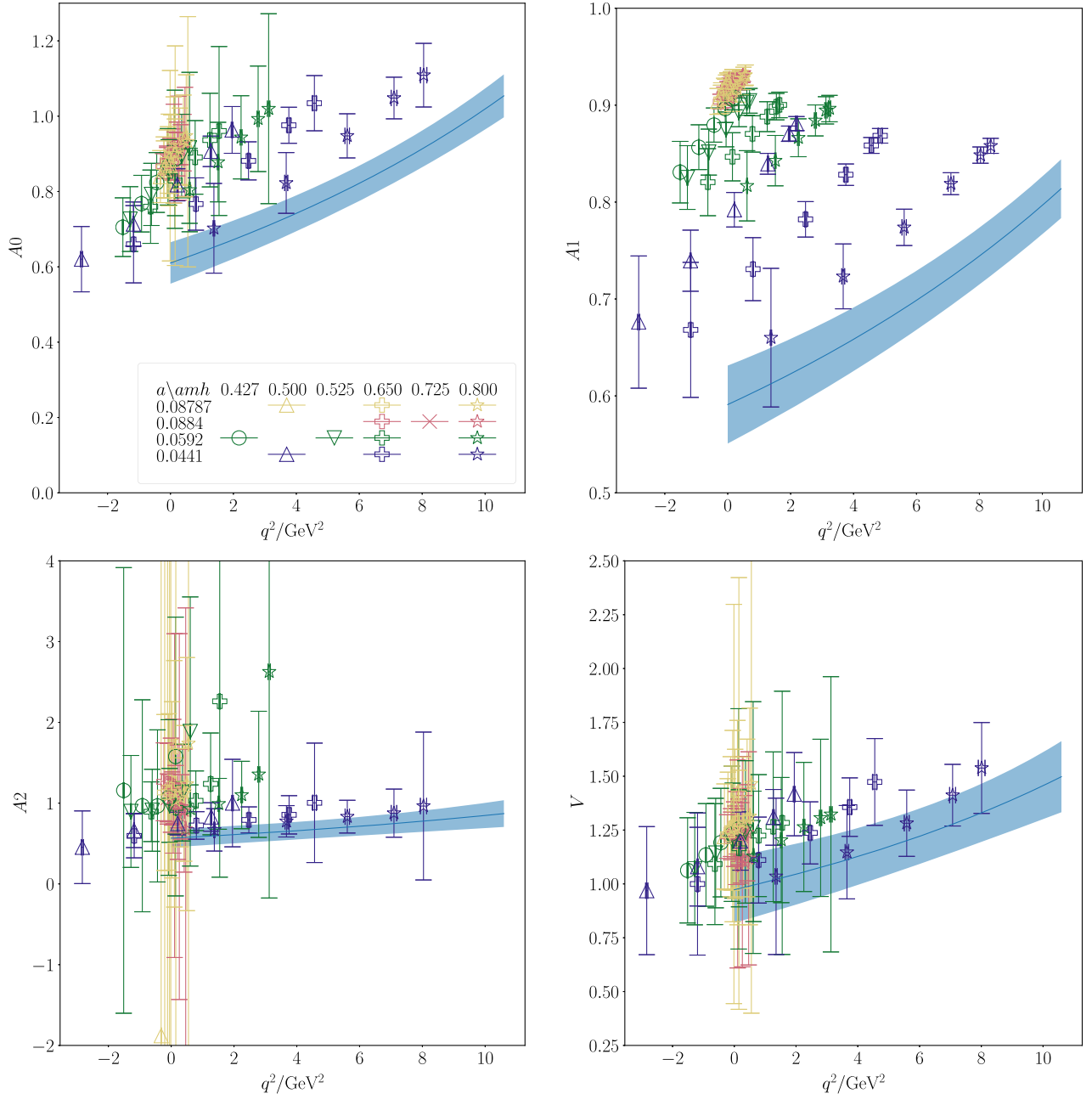


FIG. 3. The points show our lattice QCD results for each form factor as given in Tables XVIII, XIX, XX, and XXI as a function of squared four-momentum transfer, q^2 . The legend gives the mapping between symbol color and shape and the set of gluon field configurations used, as given by the lattice spacing, and the heavy quark mass in lattice units (see Tables II and III). The blue curve with error band is the result of our fit in the continuum limit and with the physical b quark mass.

We do this, using our lattice meson masses at each value of am_h and allowing for discretization and quark mass mistuning effects, by requiring

$$A_0(0) - (am_{D_s^*} + am_{H_s})/(2am_{D_s^*})A_1(0) + (am_{D_s^*} - am_{H_s})/(2am_{D_s^*})A_2(0) = \Delta_{\text{kin}}. \quad (34)$$

Δ_{kin} here is a nuisance term made up of leading-order discretization and mistuning effects to account for the use

of lattice masses rather than values in the physical continuum limit. We take

$$\Delta_{\text{kin}} = \sum_{i=1}^3 \alpha_{c,i} (am_c^{\text{val}}/\pi)^{2i} + \alpha_{h,i} (am_h/\pi)^{2i} + \beta_c \delta_{m_c}^{\text{val}} + \beta'_c \delta_{m_c}^{\text{sea}} + \beta'_s \delta_{m_s}^{\text{val}} + \beta_s \delta_{m_s}^{\text{sea}} + \beta_l \delta_{m_l}^{\text{sea}}, \quad (35)$$

where α and β are priors taken as $0(1)$. We find that the fit returns values for α and β well within their prior widths.

TABLE XIII. Physical z -expansion coefficients for the pseudoscalar, axial-vector, and vector form factors for $B_S \rightarrow D_S^*$ decay. The full correlation matrices for these coefficients are given in Appendix B.

	a_0	a_1	a_2	a_3
A0	0.1047(57)	-0.43(13)	-0.10(96)	-0.03(1.00)
A1	0.0552(21)	-0.010(54)	-0.03(77)	0.06(99)
A2	0.059(11)	-0.11(22)	-0.25(79)	-0.05(1.00)
V	0.100(11)	-0.18(27)	-0.006(0.998)	0.0(1.0)

The physical continuum form factors are given by setting $a_n = b_n^{000}$ and $\mathcal{N}_n = 1$ in Eq. (25), to give

$$F^{\text{phys}}(q^2) = \frac{1}{P(q^2)} \sum_{n=0}^3 a_n z^n, \quad (36)$$

where $P(q^2)$ is computed using the physical masses given in Table XII. These F^{phys} values are plotted in Fig. 3 together with our lattice data. The continuum values of the

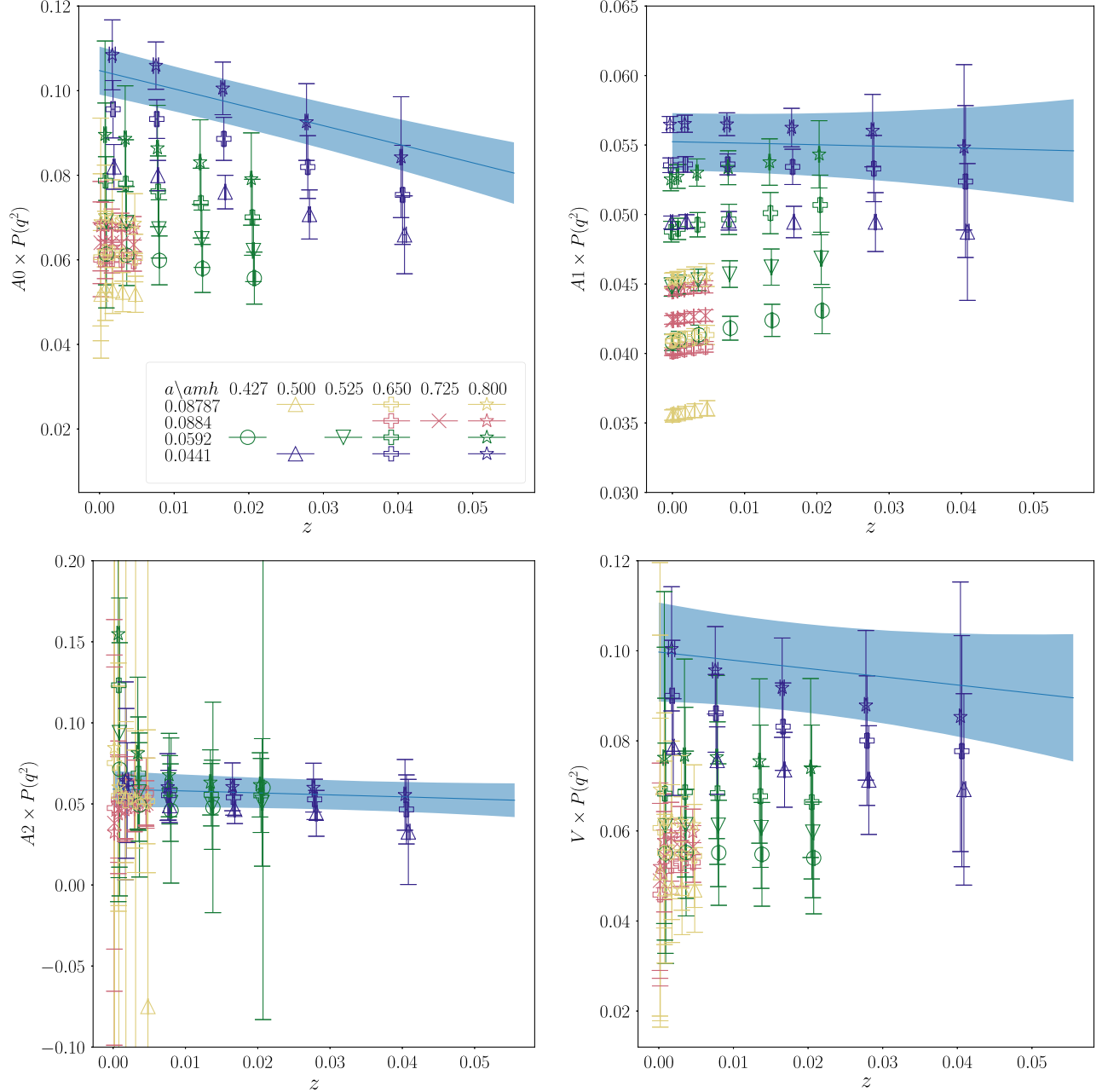


FIG. 4. The points show our lattice QCD results for each form factor as given in Tables XVIII, XIX, XX, and XXI multiplied by the pole function of Eq. (24) and plotted in z space. The legend gives the mapping between symbol color and shape and the set of gluon field configurations used, as given by the lattice spacing, and the heavy quark in lattice units (see Tables II and III). The blue curve with error band is the result of our polynomial fit in z with lattice spacing and heavy quark mass dependence [Eq. (25)], evaluating the result in the continuum limit and for the b quark mass, to give the physical form factor for $B_S \rightarrow D_S^*$.

z -expansion coefficients $a_n = b_n^{000}$ are given in Table XIII. The correlation matrices between these parameters are given in Appendix B.

In Fig. 4, we plot the form factor data, together with the extrapolated physical continuum form factors, multiplied by the pole function Eq. (24) against $z(q^2, t_0)$. There we see that the fit to the polynomial part of Eq. (25) is straightforward, with only very simple dependence on $z(q^2, t_0)$ and only mild heavy quark mass dependence. Note that here the A_1 form factor data and extrapolated curve are flatter than was found for $B_c \rightarrow J/\psi$ in Ref. [18].

B. Heavy mass dependence

Our fit results allow us to examine the physical dependence of the form factors on the heavy quark mass. This allows us to check that the dependence is relatively benign and that our fit form in Eq. (25) effectively captures this dependence.

Our fit function includes heavy mass dependence in several places. There are $\Lambda_{\text{QCD}}/M_{\eta_h}$ terms in the z -expansion coefficients, the H_s mass enters through our choice of $t_0 = q_{\text{max}}^2 = (M_{H_s} - M_{D_s^*})^2$ in the q^2 -to- z mapping, and the pole masses entering $P(q^2)$ depend on M_{H_s} . We therefore need to know how M_{H_s} varies as a function of M_{η_h} . We fit our lattice data for the $\gamma_5 \otimes \gamma_5 H_s$ against a simple function of the η_h mass. We use the function

$$M_{H_s} = (M_{\eta_h} - M_{\eta_c}^{\text{phys}})/2 + M_{D_s^*}^{\text{phys}} + \sum_{i=1}^4 X_i \left(\frac{am_h}{\pi}\right)^{2i} + \sum_{i=1}^4 Y_i \left(\frac{am_c}{\pi}\right)^{2i} + \sum_{i=1}^4 Z_i \Delta_{hc}^{(i)} + \mathcal{N}', \quad (37)$$

where

$$\Delta_{hc}^{(i)} = \left(\frac{2\Lambda_{\text{QCD}}}{M_{\eta_c}^{\text{phys}}}\right)^i - \left(\frac{2\Lambda_{\text{QCD}}}{M_{\eta_h}}\right)^i \quad (38)$$

and

$$\mathcal{N}'_n = 1 + A'_n \delta_{m_c}^{\text{val}} + B'_n \delta_{m_c}^{\text{sea}} + C'_n \delta_{m_s}^{\text{val}} + D'_n \delta_{m_s}^{\text{sea}} + E'_n \delta_{m_l}^{\text{sea}}. \quad (39)$$

This form ensures the correct value of M_{H_s} as $m_h \rightarrow m_c$. We take $M_{\eta_c}^{\text{phys}} = 2.9839$ GeV from Ref. [52], neglecting its very small uncertainty, and we also include the physical values of M_{η_b} and M_{B_s} from Ref. [52] in the fit as data points. We take prior widths of 0(1) for $A', B', C', D', E', X_i, Y_i$, and Z_i . This gives a sensible fit with $\chi^2/\text{d.o.f.} = 1.3$ and $Q = 0.2$. We then use our fitted parameters Z_i to estimate

the continuum value of M_{H_s} at a given M_{η_h} . Setting \mathcal{N}', X_i , and Y_i to zero in Eq. (37) gives

$$M_{H_s} = (M_{\eta_h} - M_{\eta_c}^{\text{phys}})/2 + M_{D_s^*}^{\text{phys}} + \sum_{i=1}^4 Z_i \Delta_{hc}^{(i)}. \quad (40)$$

Note that this parametrization of the H_s mass is only used to demonstrate the heavy mass dependence of the form factors and will not have any impact on the physical $B_s \rightarrow D_s^*$ form factors.

In Fig. 5, we plot the form factors at fixed values of the D_s^* momentum against M_{η_h} . We choose values of the D_s^* momentum which evenly span the semileptonic range at the physical b quark mass and only plot the mass region for which the resulting value of q^2 is between 0 and q_{max}^2 . We include in these plots our lattice data, connecting points on a given set which are at the same D_s^* spatial momentum. As for $B_c \rightarrow J/\psi$ [18], we see that the continuum form factors have only mild heavy mass dependence across the range of masses we use here, and that our extrapolation to the b mass using these points is reliable. This is consistent with what is seen for other $b \rightarrow c$ form factors—e.g., Refs. [16–18,53].

C. Tests of the stability of the analysis

Here, we demonstrate the stability of our analysis to the different choices of correlator fit inputs given in Table VII. We show that under these variations, the total rate of $B_s^0 \rightarrow D_s^{*-} \ell^+ \nu_\ell$ decay—i.e., $\Gamma(B_s^0 \rightarrow D_s^{*-} \ell^+ \nu_\ell) / |\eta_{\text{EW}} V_{cb}|^2 (1 + \delta_{\text{EM}})$ —is stable. This quantity is obtained by first determining the helicity amplitudes from our form factors and then integrating in q^2 over the differential rate they give [see Eqs. (4) and (3)]. The results for the differential rates and total rate will be discussed in more detail in Sec. V; here we focus on the stability of the final result under variations of fit choice.

We first look at the choices of the correlator fit parameters: $\Delta T_{3\text{pt}}$, $\Delta T_{2\text{pt}}^{D_s^*}$, $\Delta T_{2\text{pt}}^{H_s}$, the value of the SVD cut, and the number of exponentials used in the fit. In order to verify that our results are independent of such choices, we repeat the full analysis using all combinations of the variations listed in Table VII. The total rate computed using each of these fit variations is plotted in Fig. 6, where we see that our final result is not sensitive to such variations.

We also look at the dependence of the physical continuum z -expansion coefficients, $a_n = b_n^{000}$, on these variations [see Eq. (25)]. In Fig. 7, we show the variation of the fitted a_0 coefficient for the form factors V and A_1 , as well as the a_1 term for A_1 . In these plots, we see that these coefficients are very stable to variations of correlator fit inputs.

We also show that the form factors themselves are stable under these variations. In Figs. 8 and 9, we show the

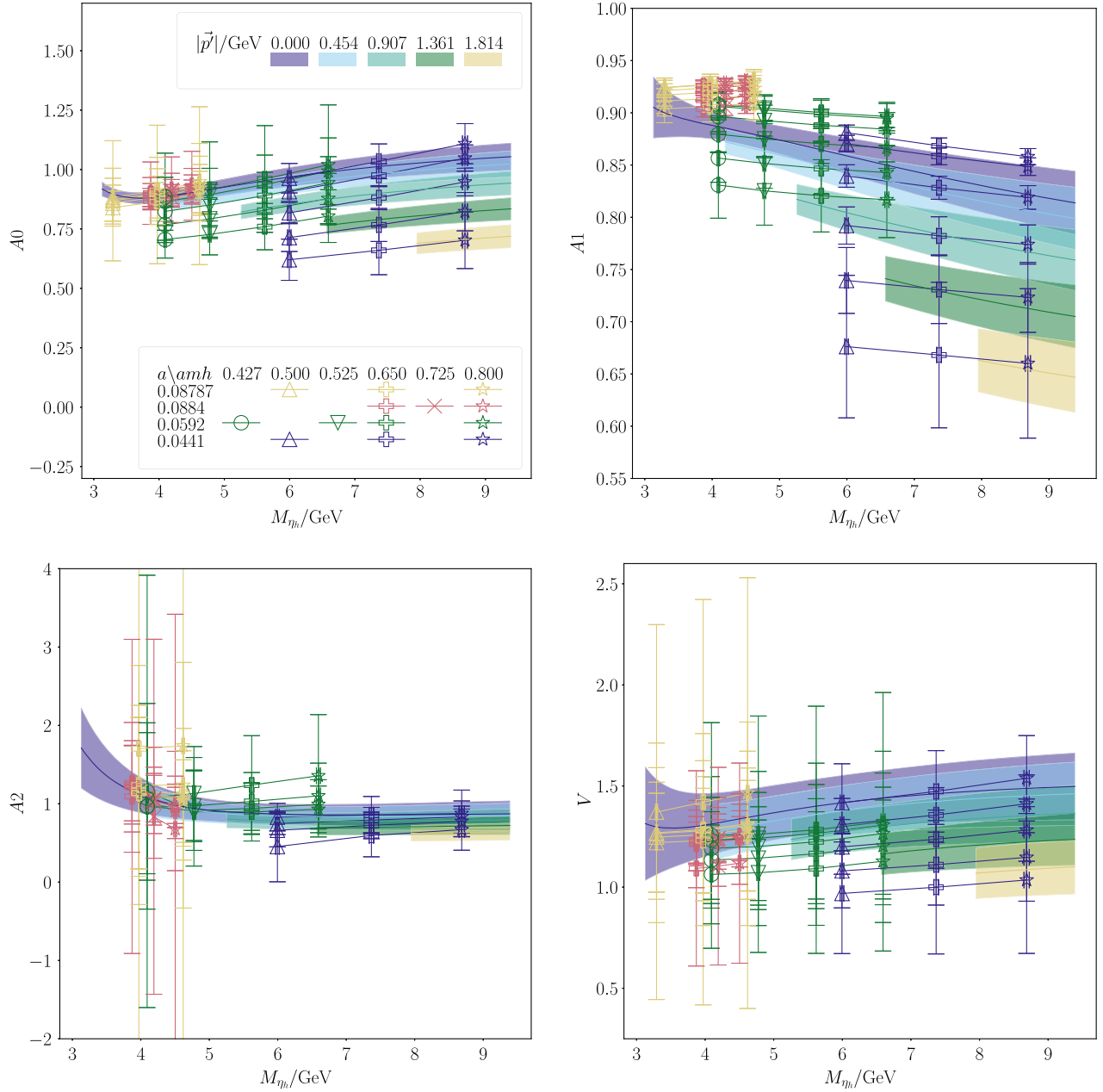


FIG. 5. The points show our lattice QCD results for each form factor as given in Tables XVIII, XIX, XX, and XXI as a function of the η_h mass M_{η_h} , with data points corresponding to the same D_S^* spatial momentum (given in Tables XVIII to XXI) connected. We also use Eq. (40) to plot our continuum result (solid colored curves) at multiple, evenly spaced, fixed values of D_S^* momentum within the semileptonic region $0 \leq q^2 \leq q_{\max}^2$. The legend gives the mapping between the symbol color and shape and the set of gluon field configurations, as given by the lattice spacing, and the heavy quark in lattice units (see Tables II and III). Note that for the form factor A_2 , we exclude from the plot the inaccurate lattice data for $am_h = 0.5$ on Set 4, as well as $ak = 0.059$ and $ak = 0.052$ on Sets 2 and 3, respectively.

variation of the form factors V and A_1 , evaluated at $q^2 = 1 \text{ GeV}^2$, 5 GeV^2 , and 10 GeV^2 , where we see that A_1 and V are very stable to variations of correlator fit inputs. Similar plots for A_0 and A_2 are given in Sec. 1 of Appendix D.

We also convert our results to the Boyd, Grinstein, and Lebed (BGL) scheme [38] and check the unitarity

constraints. This analysis is given in Sec. 1 of Appendix C, where we see that these constraints are far from saturation. In Ref. [18], we also studied the effect of including fewer resonances in the pole term [Eq. (24)]. Here, in addition to this analysis, we also investigate using alternative parametrizations when performing the heavy-HISQ fit. We show the results of these fits in Appendix D,

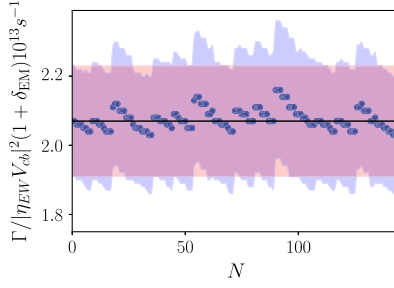


FIG. 6. Plot showing the stability of the total rate for $B_s^0 \rightarrow D_s^{*-} \mu^+ \nu_\mu$ under variations of the correlator fits. The x -axis value corresponds to $N = \delta_3 + 4\delta_2 + 16\delta_1 + 64\delta_4$, where δ_n is the value of δ corresponding to the fit given in Table VII for set n . The black horizontal line and red error band correspond to our final result, and the blue points and blue error band correspond to the combination of fit variations associated to N . Our result for the total rate does not change significantly for these variations in the fits. Note that here we do not include the contribution of δ_{EM} to the uncertainty.

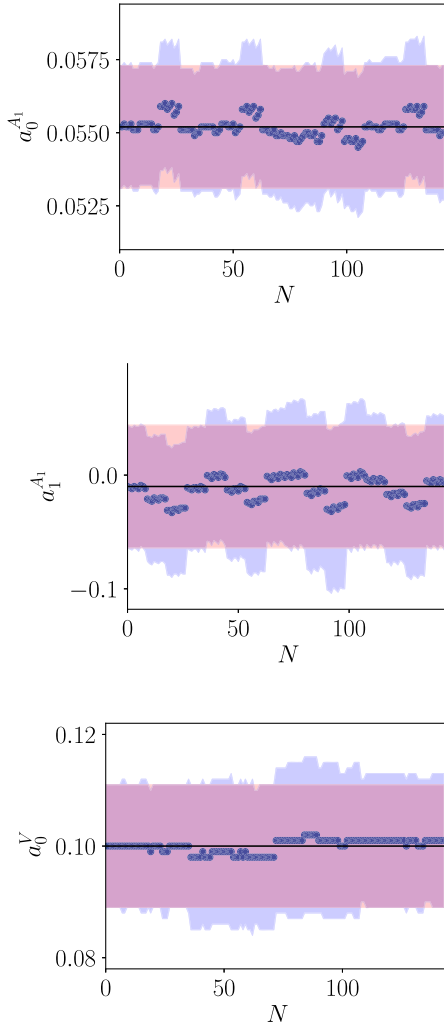


FIG. 7. As for Fig. 6, showing the stability of the coefficients of the z expansion for the form factors under variations of the correlator fits. We include a subset of coefficients here; other plots look very similar.

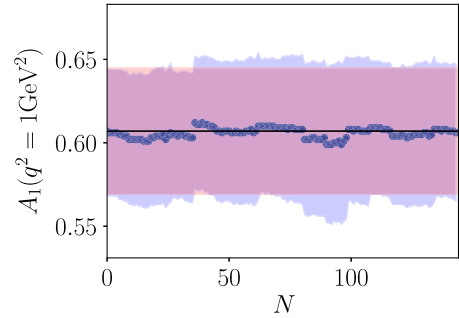
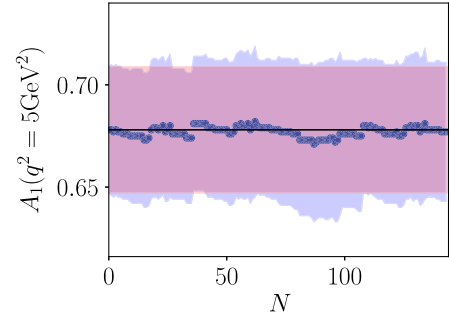
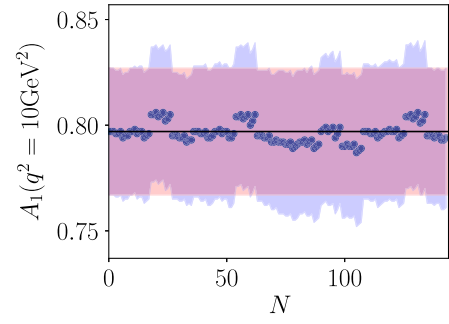


FIG. 8. As for Fig. 6, showing the stability of the form factor A_1 evaluated at $q^2 = 1 \text{ GeV}^2$, 5 GeV^2 , and 10 GeV^2 .

where we see no significant variation in the physical form factors or differential decay rate.

V. DISCUSSION OF LATTICE RESULTS

A. Differential and total rates for each lepton flavor

In this section, we first use our form factors to construct the helicity amplitudes defined in Eq. (4). These are plotted in Fig. 10, where we see that $H_0(q_{\text{max}}^2) = H_\pm(q_{\text{max}}^2)$ and that H_0 and H_t are singular at $q^2 = 0$, as we would expect from the factors of $1/\sqrt{q^2}$ appearing in their definitions. This singular behavior is canceled in the physical differential decay rate by the factor of $(q^2 - m_\ell^2)^2$ appearing in Eq. (2).

From these helicity amplitudes we compute the differential rate with respect to q^2 , given by Eq. (3). This is plotted in Fig. 11 for the $\ell = \mu$ and $\ell = \tau$ cases, where in the plot we normalize both curves by the total rate Γ for the

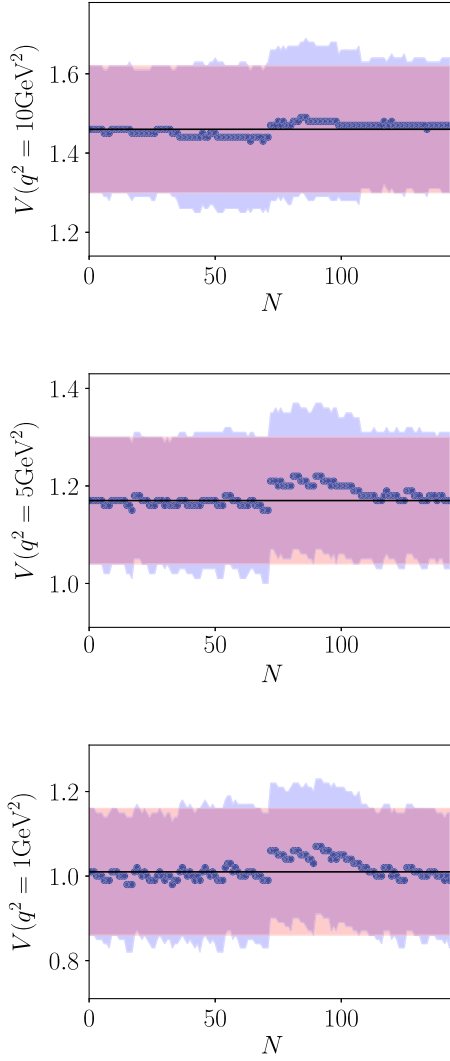


FIG. 9. As for Fig. 6, showing the stability of the form factor V evaluated at $q^2 = 1 \text{ GeV}^2$, 5 GeV^2 , and 10 GeV^2 .

$\ell = \mu$ case. We integrate these, as well as the rate for $\ell = e$, to find the total rate for each lepton flavor. When integrating our results, we use a simple (but accurate) trapezoidal approximation in order to ensure we carry through correlations correctly. We find

$$\begin{aligned} \frac{\Gamma(B_S^0 \rightarrow D_S^{*-} e^+ \nu_e)}{|\eta_{EW} V_{cb}|^2} &= 2.07(17)_{\text{latt}}(2)_{\text{EM}} \times 10^{13} \text{ s}^{-1} \\ &= 13.6(1.1)_{\text{latt}}(0.1)_{\text{EM}} \times 10^{-12} \text{ GeV} \end{aligned} \quad (41)$$

and

$$\begin{aligned} \frac{\Gamma(B_S^0 \rightarrow D_S^{*-} \mu^+ \nu_\mu)}{|\eta_{EW} V_{cb}|^2} &= 2.06(16)_{\text{latt}}(2)_{\text{EM}} \times 10^{13} \text{ s}^{-1} \\ &= 13.6(1.1)_{\text{latt}}(0.1)_{\text{EM}} \times 10^{-12} \text{ GeV} \end{aligned} \quad (42)$$

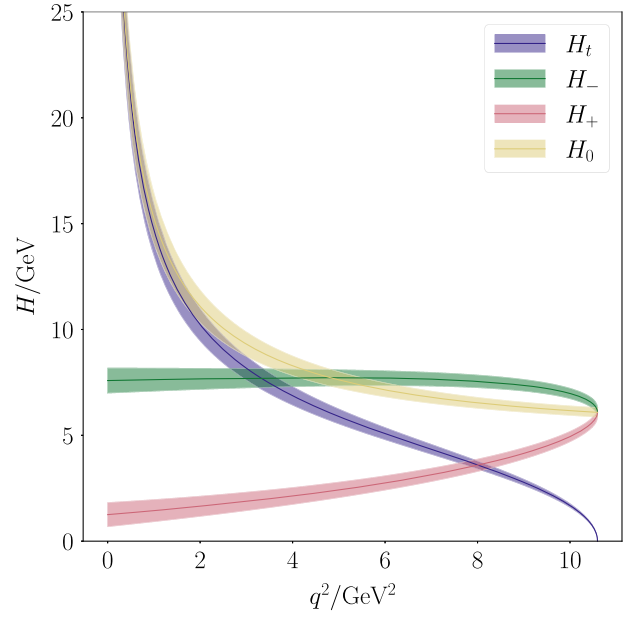


FIG. 10. Helicity amplitudes for $B_S \rightarrow D_S^*$ plotted as a function of q^2 .

with the ratio $\Gamma_{\ell=e}/\Gamma_{\ell=\mu} = 1.00443(16)$, amounting to an effect of 0.4% in the total rate from the muon mass. Note that we are ignoring differences in δ_{EM} between the two cases in this ratio. For the $\ell = \tau$ case, the effect of including the mass is much more substantial, and we find

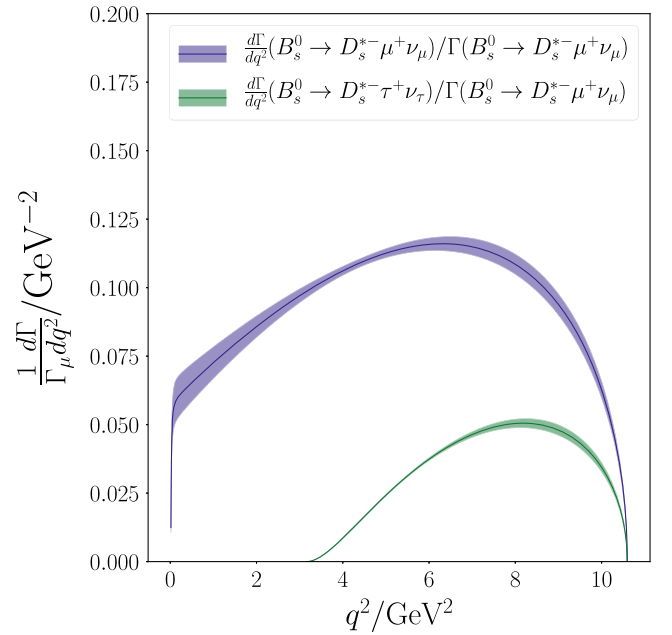


FIG. 11. The differential rate $d\Gamma/dq^2$ for $B_S^0 \rightarrow D_S^{*-} \ell^+ \nu_\ell$ for $\ell = \mu$ and $\ell = \tau$ as a function of q^2 , normalized by the total decay rate for the $\ell = \mu$ case. Note that here, for the $\ell = \tau$ curve, the error bands do not include the contribution from δ_{EM} .

$$\begin{aligned} \frac{\Gamma(B_s^0 \rightarrow D_s^{*-} \tau^+ \nu_\tau)}{|\eta_{\text{EW}} V_{cb}|^2} &= 5.14(37)_{\text{latt}}(5)_{\text{EM}} \times 10^{12} \text{ s}^{-1} \\ &= 3.38(24)_{\text{latt}}(3)_{\text{EM}} \times 10^{-12} \text{ GeV}. \end{aligned} \quad (43)$$

We can also readily construct $R(D_s^*)$, the ratio of the total rates for the $\ell = \tau$ and $\ell = \mu$ cases, where many uncertainties which are correlated between the two cancel. We find

$$R(D_s^*) = \Gamma_{\ell=\tau}/\Gamma_{\ell=\mu} = 0.2490(60)_{\text{latt}}(35)_{\text{EM}}. \quad (44)$$

This value is $\approx 1.6\sigma$ below the value of $R(J/\psi)$ computed in Ref. [19], as well as the HFLAV average SM value of $R(D^*)$ [1]. Note that our value is consistent with the value computed in Ref. [54] using the heavy-quark expansion of $R(D_s^*) = 0.2472(77)$. Note also that unlike the total rate Γ , for which the contribution of δ_{EM} to the uncertainty is relatively small, the lattice uncertainty in $R(D_s^*)$ is the same order of magnitude as the uncertainty resulting from long-range QED effects, at least for charged final-state mesons. These QED effects are often ignored but must be addressed in future calculations in order to produce reliable SM results with subpercent-level uncertainties.

We also construct the improved ratio [55]

$$R^{\text{imp}}(D_s^*) = \frac{\int_{m_\tau^2}^{q_{\text{max}}^2} dq^2 \frac{d\Gamma}{dq^2}(B_s^0 \rightarrow D_s^{*-} \tau^+ \nu_\tau)}{\int_{m_\tau^2}^{q_{\text{max}}^2} dq^2 \frac{d\Gamma}{dq^2}(B_s^0 \rightarrow D_s^{*-} \mu^+ \nu_\mu)}. \quad (45)$$

We find

$$R^{\text{imp}}(D_s^*) = 0.3324(31)_{\text{latt}}(47)_{\text{EM}}, \quad (46)$$

where now the uncertainty resulting from electromagnetic effects is dominant due to the improved cancellation of correlated lattice uncertainties.

We may use our value of $\Gamma/|\eta_{\text{EW}} V_{cb}|^2$ in Eq. (42), together with values of V_{cb} and η_{EW} , to derive a result for the total width of the decay. We take $\eta_{\text{EW}} = 1.0066$ following Ref. [56] and $|V_{cb}| = 41.0(1.4) \times 10^{-3}$ using an average of inclusive and exclusive determinations with the error scaled by 2.4 to allow for their inconsistency [52]. Note that here we neglect the small uncertainty in η_{EW} . This gives

$$\Gamma(B_s^0 \rightarrow D_s^{*-} \mu^+ \nu_\mu) = 3.53(27)_{\text{latt}}(24)_{V_{cb}}(4)_{\text{EM}} \times 10^{10} \text{ s}^{-1}, \quad (47)$$

where the first uncertainty is from our lattice QCD calculation, the second is from the uncertainty in $|V_{cb}|$, and the final error is from δ_{EM} . We may combine this with the experimental average of the B_s^0 mean lifetime [1,52], $\tau(B_s^0) = 1.515(4) \times 10^{-12}$ s, to find the branching fraction

$$\text{Br}(B_s^0 \rightarrow D_s^{*-} \mu^+ \nu_\mu) = 0.0534(42)_{\text{latt}}(36)_{V_{cb}}(1)_\tau(5)_{\text{EM}}, \quad (48)$$

where the uncertainties are from our lattice calculation, from the uncertainty in V_{cb} , from the uncertainty in the B_s^0 lifetime, and from δ_{EM} , respectively. This is in good agreement with, but much more accurate than, the value of the more inclusive branching fraction measured by Belle, $\text{Br}(B_s^0 \rightarrow D_s^{*-} X \ell^+ \nu) = 0.054(11)$ [57].

B. Angular and polarization asymmetries and ratios

We can also construct the lepton polarization asymmetry, as well as the longitudinal polarization fraction and the forward-backward asymmetry. Note that as for $B \rightarrow D^*$ [10] and $B_c \rightarrow J/\psi$ [19], these are conventionally defined for the charge conjugate mode, which here is $\bar{B}_s^0 \rightarrow D_s^{*+} \ell^- \bar{\nu}_\ell$. They are given by

$$\begin{aligned} \mathcal{A}_{\lambda_\ell}(q^2) &= \frac{d\Gamma^{\lambda_\ell=-1/2}/dq^2 - d\Gamma^{\lambda_\ell=+1/2}/dq^2}{d\Gamma/dq^2}, \\ F_L^{D_s^*}(q^2) &= \frac{d\Gamma^{\lambda_{D_s^*}=0}/dq^2}{d\Gamma/dq^2}, \\ \mathcal{A}_{FB}(q^2) &= \frac{1}{d\Gamma/dq^2} \frac{2}{\pi} \int_0^\pi \frac{d\Gamma}{dq^2 d\cos(\theta_W)} \cos(\pi - \theta_W) d\theta_W, \end{aligned} \quad (49)$$

respectively, where we have chosen the forward direction for the purpose of \mathcal{A}_{FB} as being in the direction of the D_s^* momentum in the B_s rest frame. We plot these for the $\ell = \mu$ and $\ell = \tau$ cases in Fig. 12. Following the notation used in Refs. [10,19] for the integrated observables and lepton-flavor-universality-violating ratios, we find for the $\ell = \tau$ case

$$\begin{aligned} \langle \mathcal{A}_{\lambda_\tau} \rangle &= 0.520(12), \\ \langle F_L^{D_s^*} \rangle &= 0.440(16), \\ \langle \mathcal{A}_{FB} \rangle &= -0.092(24). \end{aligned} \quad (50)$$

Note that these are consistent with the values given in Ref. [54] of $\langle F_L^{D_s^*} \rangle = 0.471(16)$ and $\langle \mathcal{A}_{\lambda_\tau} \rangle = 0.486(23)$. For the ratios of $\ell = \tau$ to $\ell = \mu$ cases, we find

$$\begin{aligned} R(\mathcal{A}_{\lambda_\tau}) &= 0.524(12), \\ R(F_L^{D_s^*}) &= 0.880(18), \\ R(\mathcal{A}_{FB}) &= 0.345(56). \end{aligned} \quad (51)$$

C. Ratio of $B_s \rightarrow D_s$ and $B_s \rightarrow D_s^*$ rates

We may also use our results in combination with the results of Ref. [16] to compute the ratio $\Gamma(B_s^0 \rightarrow D_s^- \mu^+ \nu_\mu)/\Gamma(B_s^0 \rightarrow D_s^{*-} \mu^+ \nu_\mu)$. In doing so, we neglect correlations between the two calculations. Note that here, as for $R(D_s^*)$, the $|\eta_{\text{EW}} V_{cb}|^2$ factors cancel in the

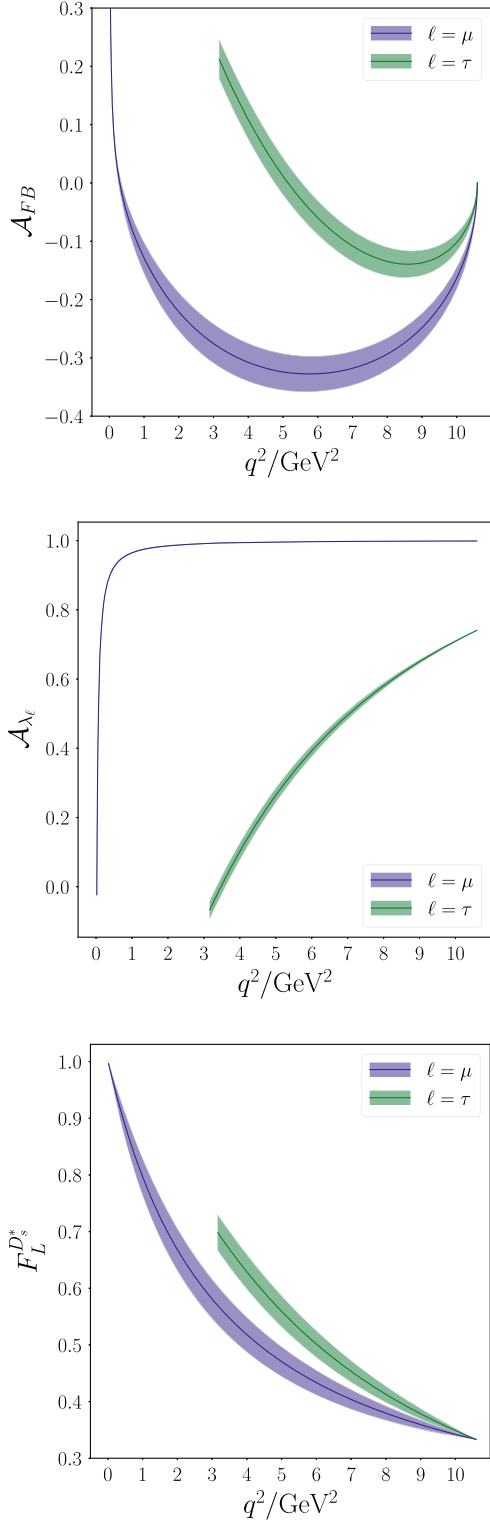


FIG. 12. Angular asymmetry variables for $\bar{B}_S^0 \rightarrow D_S^{*+} \ell^- \bar{\nu}_\ell$ decay defined in Eq. (49) for the cases $\ell = \mu$ and $\ell = \tau$.

ratio. The uncertainty in $\Gamma(B_S \rightarrow D_S)$ computed using the results in Ref. [16], $\Gamma(B_S \rightarrow D_S)/|\eta_{EW} V_{cb}|^2 = 6.02(24) \times 10^{-12}$ GeV, is a factor of ≈ 2 smaller than the uncertainty in $\Gamma(B_S \rightarrow D_S^*)$, and the correlations between

TABLE XIV. Error budget for the total rate Γ for the cases $\ell = \mu$ and $\ell = \tau$, given in Eqs. (42) and (43), respectively, as well as for $R(D_S^*)$, given in Eq. (44), excluding the contribution from δ_{EM} . Errors are given as a percentage of the final answer. The top half gives the contributions of systematic uncertainties originating from the dependence of the form factors on M_{η_h} , from discretization effects going as am_h and am_c , from sea and valence quark mass mistunings, and from uncertainties in the determination of the lattice spacing. The second half of the table gives the contributions of the statistical uncertainty in our lattice correlator data, broken down by set. Finally, ‘‘Other priors’’ includes all of the remaining sources of uncertainty, such as Δ_{kin} and the current renormalization factors. ‘‘Other priors’’ also includes the uncertainty of mixed terms in the fit which cannot be attributed uniquely to any of the categories in the first half of the table (e.g., from the prior uncertainty of b_n^{011} , the coefficient in Eq. (25) which mixes am_h and am_c dependence).

Source	$\Gamma/ \eta_{EW} V_{cb} ^2(1 + \delta_{EM})$		$R(D_S^*)$
	$\ell = \mu$	$\ell = \tau$	
$M_{\eta_h} \rightarrow M_{\eta_b}$	2.62	2.26	1.12
$am_c \rightarrow 0$	2.0	1.8	0.3
$am_h \rightarrow 0$	3.7	3.6	0.52
$\delta_{m_c}^{val}$	0.20	0.18	0.058
$\delta_{m_c}^{sea}$	2.2	2.3	0.087
$\delta_{m_s}^{val}$	0.02	0.02	0.01
$\delta_{m_s}^{sea}$	1.1	1.1	0.03
$\delta_{m_l}^{sea}$	0.75	0.71	0.10
$w_0/a, w_0$	0.46	0.54	0.17
Statistics			
Set 1	1.3	1.0	0.51
Set 2	2.5	2.2	0.76
Set 3	4.3	3.6	1.6
Set 4	0.69	0.51	0.26
Other priors	2.3	2.1	0.88
Total	8.0	7.2	2.4

the two results are expected to be relatively small. Neglecting these correlations is therefore not expected to significantly affect the uncertainty in the ratio. We find

$$\frac{\Gamma(B_S^0 \rightarrow D_S^- \mu^+ \nu_\mu)}{\Gamma(B_S^0 \rightarrow D_S^{*-} \mu^+ \nu_\mu)} = 0.443(40)_{\text{lat}}(4)_{\text{EM}}. \quad (52)$$

This is in good agreement with the experimental value of $\Gamma(B_S^0 \rightarrow D_S^- \mu^+ \nu_\mu)/\Gamma(B_S^0 \rightarrow D_S^{*-} \mu^+ \nu_\mu) = 0.464(45)$ recently measured by LHCb [6] and has a comparable uncertainty.

D. Error budget

We use the **lsqfit** [58] inbuilt error budget function, which computes the partial variance of our result with respect to priors and data, to estimate the contributions of systematic uncertainties (see, e.g., Appendix A of Ref. [59]). The error budget for the total rate Γ , for both

TABLE XV. w bins together with normalized integrated rates for $B_s^0 \rightarrow D_s^{*-} \mu^+ \nu_\mu$ for each bin. The row labeled “This work” gives those values computed using our form factors, discussed in the text, and the LHCb values are those given in Ref. [56]. These are in reasonable agreement, with $\chi^2/\text{d.o.f.} = 1.8$ and a Q -value of 0.1. Note that the majority of the tension with our results originates from the LHCb value for the bin $1.1688 < w < 1.2212$.

w bin		1.0–1.1087	1.1087–1.1688	1.1688–1.2212	1.2212–1.2717	1.2717–1.3226	1.3226–1.3814	1.3814–1.4667
$\Gamma_{\text{bin}}/\Gamma_{\text{tot}}$	This work	0.1946(82)	0.1537(45)	0.1381(29)	0.1291(18)	0.1213(19)	0.1243(40)	0.139(11)
	LHCb [56]	0.183(12)	0.1440(84)	0.1480(76)	0.1280(77)	0.1170(69)	0.1220(62)	0.1580(93)

the $\ell = \mu$ and $\ell = \tau$ cases, excluding the contribution from δ_{EM} , is given in Table XIV together with the budget for $R(D_s^*)$. We see here, as we would expect from Ref. [19], that the largest uncertainties originate from the statistics on Set 3, from taking $am_h \rightarrow 0$ and from taking $M_{\eta_h} \rightarrow M_{\eta_b}$.

Note that these uncertainties may also be straightforwardly and systematically improved, as discussed in Ref. [19]. The key improvements would be to include more gluon field configurations to reduce the statistical errors on the current finest Set 3. Adding in results from “exafine” lattices with $a \approx 0.03$ fm is also feasible. These would allow for calculations directly at the physical b -quark mass with $am_h \approx 0.6$ [23], reducing the uncertainties associated with taking $am_h \rightarrow 0$ and $M_{\eta_h} \rightarrow M_{\eta_b}$ significantly.

VI. COMPARISON TO LHCb RESULTS FOR THE DIFFERENTIAL DECAY RATE

A. The shape of the differential decay rate

The predicted shape of the differential rate $d\Gamma/dq^2$ from our form factors, plotted in Fig. 11, may be compared directly to recent experimental measurements by LHCb. The results of these measurements are given in Ref. [56], where unfolded normalized data are binned according to the recoil parameter, $w = v_{B_s} \cdot v_{D_s^*}$, and include correlations. Here, $v_{D_s^*}$ and v_{B_s} are the four-velocities of D_s^* and B_s , respectively. In the B_s rest frame, this gives the simple form $w = E_{D_s^*}(p')/M_{D_s^*} = (M_{B_s}^2 + M_{D_s^*}^2 - q^2)/(2M_{B_s}M_{D_s^*})$. Here we integrate our computed differential rate normalized by the total rate over the bins used in Ref. [56]. The w limits of these bins, together with our integrated normalized rates for each bin, are given in Table XV together with the measured values from LHCb.

Our results and those of LHCb are plotted together in Fig. 13. We see that our results largely agree with the LHCb measurement. We compute the value of $\chi^2/\text{d.o.f.}$ for these measured values compared to our predicted values in the usual way, using $\chi^2 = \delta g \sigma^{-1} \delta g$, where the vector δg is made up of the differences between our values and the measured values, and σ^{-1} is the inverse of the covariance matrix for δg , including correlations from this calculation and those from experiment. We find $\chi^2/\text{d.o.f.} = 1.8$ with a Q -value of 0.1. In Fig. 13, we see that the third bin with $1.1688 < w < 1.2212$ seems to be the furthest from our predicted rate. Excluding this bin from the computation of

$\chi^2/\text{d.o.f.}$ results in a $\chi^2/\text{d.o.f.}$ of 0.62, with a Q -value of 0.78.

For comparison to others, it is useful to give our results in the Caprini, Lellouch, and Neubert (CLN) form factor parametrization [39]. In this scheme, the form factors are rewritten in terms of a single leading form factor h_{A_1} together with three ratios. These are related to our form factors by

$$\begin{aligned}
 h_{A_1}(w) &= A_1(w) \frac{2}{w+1} \frac{1}{R_{D_s^*}}, \\
 R_0(w) &= A_0(w) \frac{R_{D_s^*}}{h_{A_1}(w)}, \\
 R_1(w) &= V(w) \frac{R_{D_s^*}}{h_{A_1}(w)}, \\
 R_2(w) &= A_2(w) \frac{R_{D_s^*}}{h_{A_1}(w)},
 \end{aligned} \tag{53}$$

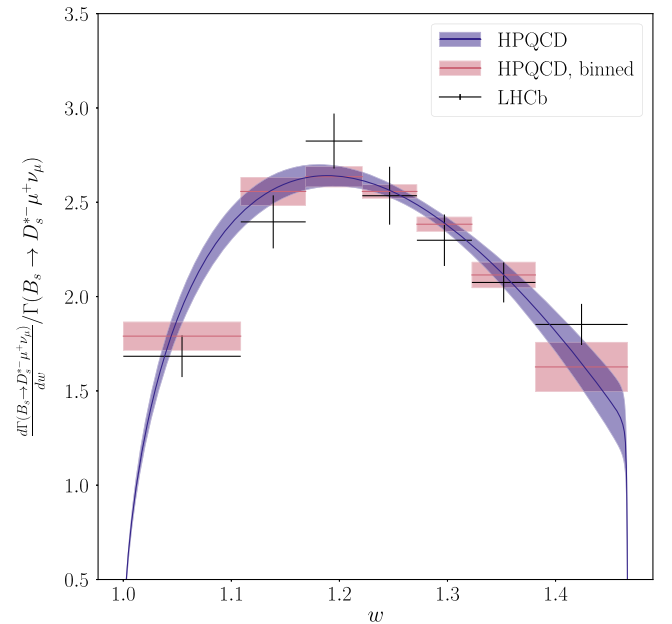


FIG. 13. The differential rate $d\Gamma/dw$ for $B_s^0 \rightarrow D_s^{*-} \mu^+ \nu_\mu$ as a function of the recoil $w = v_{B_s} \cdot v_{D_s^*}$ and normalized by the total decay rate calculated from our form factors is given by the purple band. We also show our rate integrated across bins and measurements by LHCb [56].

where $R_{D_S^*} = 2\sqrt{r}/(1+r)$, with $r = M_{D_S^*}/M_{B_S}$. These are then parametrized as

$$\begin{aligned}
 h_{A_1}(w) &= h_{A_1}(1)[1 - 8\rho^2 z(w) + (53\rho^2 - 15)z^2(w) \\
 &\quad - (231\rho^2 - 91)z^3(w)], \\
 R_0(w) &= R_0(1) - 0.11(w-1) + 0.01(w-1)^2, \\
 R_1(w) &= R_1(1) - 0.12(w-1) + 0.05(w-1)^2, \\
 R_2(w) &= R_2(1) + 0.11(w-1) - 0.06(w-1)^2, \quad (54)
 \end{aligned}$$

where the expressions for $h_{A_1}(w)$, $R_1(w)$, and $R_2(w)$ may be found in Ref. [39], and the expression for $R_0(w)$ is derived from the results of Ref. [39] in Ref. [60]. In this case,

$$z(w) = \frac{\sqrt{w+1} - \sqrt{2}}{\sqrt{w+1} + \sqrt{2}}, \quad (55)$$

and $h_{A_1}(1)$, $R_0(1)$, $R_1(1)$, $R_2(1)$, and ρ^2 are the free parameters. Converting our continuum form factor results to this scheme and then fitting the CLN parameters gives

$$\begin{aligned}
 h_{A_1}(1) &= 0.902(36), \\
 R_0(1) &= 1.057(58), \\
 R_1(1) &= 1.52(16), \\
 R_2(1) &= 0.93(11), \\
 \rho^2 &= 1.23(12). \quad (56)
 \end{aligned}$$

The value of ρ^2 may be compared to the LHCb experimental result given in Ref. [56], $\rho_{\text{exp}}^2 = 1.16(9)$, and we see that our result is in good agreement. In Ref. [56], the term $h_{A_1}(1)$ is absorbed into the normalization, and values for $R_1(1)$ and $R_2(1)$ are taken from the HFLAV average of the corresponding parameters determined from experimental measurements of $B \rightarrow D^*$ decay [1]. These are given by

$$\begin{aligned}
 R_1^{B \rightarrow D^*}(1) &= 1.270(26), \\
 R_2^{B \rightarrow D^*}(1) &= 0.852(18). \quad (57)
 \end{aligned}$$

Reference [1] also gives $\rho_{B \rightarrow D^*}^2 = 1.122(24)$. Our results agree with these values within uncertainties, and so we see no significant $SU(3)_{\text{flavor}}$ symmetry breaking between the measured shape of $B \rightarrow D^*$ decay and our results for $B_S \rightarrow D_S^*$ using the CLN parametrization scheme. We may also compare our values to those measured by LHCb in Ref. [6]: $\rho^{2,\text{LHCb}} = 1.23(17)$, $R_1^{\text{LHCb}}(1) = 1.34(25)$, and $R_2^{\text{LHCb}}(1) = 0.83(16)$, where again we see good agreement.

We may also compare our result for $R_0(1)$ to the value for $B \rightarrow D^*$ decays, which is suppressed by a factor

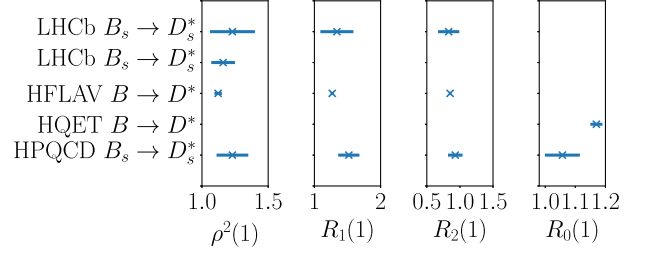


FIG. 14. Plot comparing our results for the CLN shape parameters ρ^2 , $R_1(1)$, $R_2(1)$, and $R_0(1)$ to those determined by LHCb in Refs. [6,56]. We also include in this figure the HFLAV values for the $B \rightarrow D^*$ shape parameters [1], as well as the HQET result for $R_0(1)$ for $B \rightarrow D^*$ [61]. We see good agreement, except for our value of $R_0(1)$, which is in slight tension with the HQET result.

of m_ℓ^2/q^2 in experimentally measured rates, and so is instead determined from HQET [61]. We find this value, $R_0^{B \rightarrow D^*,\text{HQET}}(1) = 1.17(2)$, is in slight tension with our result, with the central value higher by $\approx 1.5\sigma$. These comparisons to experiment and HQET results are summarized in Fig. 14.

B. Determination of $|V_{cb}|$

In this section, we use the results of Ref. [6] to reconstruct LHCb's measured differential decay rate, using the CLN parametrization scheme, and then compare this to our results here in order to extract a value of $|V_{cb}|$. We use the values of ρ^2 , $R_1(1)$, $R_2(1)$, η_{EW} , $h_{A_1}(1)$, and $|V_{cb}|$ given in Ref. [6], including their correlations, to reconstruct the measured differential rate, $d\Gamma^{\text{exp}}/dq^2$, parametrized in the CLN scheme. We then fit this using our computed $(1/|V_{cb}\eta_{\text{EW}}|^2)d\Gamma/dq^2$ in order to extract a value of $|V_{cb}|$. We find

$$|V_{cb}|^{\text{CLN}} = 41.6(1.5)_{\text{latt}}(1.6)_{\text{exp}}(0.4)_{\text{EM}} \times 10^{-3}, \quad (58)$$

where the first uncertainty is from our form factor calculation, the second is from the uncertainty in $d\Gamma^{\text{exp}}/dq^2$, and the final uncertainty is from δ_{EM} .

Repeating this analysis using the BGL parameters given in Ref. [6] to reconstruct $d\Gamma^{\text{exp}}/dq^2$ yields a value of

$$|V_{cb}|^{\text{BGL}} = 42.7(1.5)_{\text{latt}}(1.7)_{\text{exp}}(0.4)_{\text{EM}} \times 10^{-3}, \quad (59)$$

where again the first uncertainty is from our form factors and the second is from the uncertainty in $d\Gamma^{\text{exp}}/dq^2$. Note that the difference between $|V_{cb}|^{\text{BGL}}$ and $|V_{cb}|^{\text{CLN}}$ is compatible with the difference between $|V_{cb}|$ determined using the two schemes observed in Ref. [6], using just the zero recoil lattice result, $h_{A_1}(1)$, from Refs. [3,17].

Since the fits to both the CLN and BGL schemes in Ref. [6] have similar $\chi^2/\text{d.o.f.}$'s, we take the average

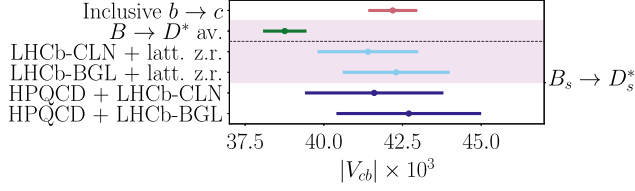


FIG. 15. Comparison of results for $|V_{cb}|$. The values obtained using our lattice results across the full physical q^2 range and LHCb results parametrized using the BGL and CLN schemes given in Ref. [6] are shown in dark blue. We plot the values determined by LHCb [6], using BGL and CLN parametrizations and lattice input only at zero recoil, in light blue. We also show the average value determined using $B \rightarrow D^{(*)}$ decay, again with lattice results at zero recoil only, in green, and the value determined from inclusive $b \rightarrow c$ measurements in red. Both of these latter values are taken from Ref. [1]. The pink shaded band indicates which results use lattice input only at zero recoil.

central value of $|V_{cb}|^{\text{BGL}}$ and $|V_{cb}|^{\text{CLN}}$, together with the larger of the two uncertainties from Eq. (59), to give

$$|V_{cb}| = 42.2(1.5)_{\text{latt}}(1.7)_{\text{exp}}(0.4)_{\text{EM}} \times 10^{-3}. \quad (60)$$

The uncertainty is split approximately equally between lattice QCD and experiment.

We show a comparison of our results to those of Ref. [6], together with the average values computed using $B \rightarrow D^{(*)}$ decay and from $b \rightarrow c$ inclusive measurements, both taken from Ref. [1], in Fig. 15. Our result from this first calculation is not sufficiently accurate to resolve the long-standing tension between the inclusive and exclusive V_{cb} results.

We see from Fig. 15 that a model-independent determination of $|V_{cb}|$ using $B_s \rightarrow D_s^*$ will require a reduction in uncertainty by a factor of ≈ 3 to reach the same precision as that quoted for the exclusive determination using $B \rightarrow D^*$ at zero recoil. This reduction is feasible with a direct comparison of improved lattice and experimental results that would enable a joint fit. Here we have used experimental results indirectly, through the fitted BGL and CLN parameters provided by LHCb in Ref. [6]. Fitting our results directly to binned experimental data for $d\Gamma/dq^2$ would reduce or remove dependence on the parametrization scheme used by the experiment and would certainly be preferable if these data were available. A similar comparison of future lattice results for the $B \rightarrow D^*$ differential rate against binned experimental values will be important for determining V_{cb} with reduced dependence on the parametrization scheme used.

C. Determining $d\mathcal{F}(w)/dw|_{w=1}$

After integrating over the angular variables, the differential rate with respect to the recoil w for $B_{(s)} \rightarrow D_{(s)}^*$ may be written [39]

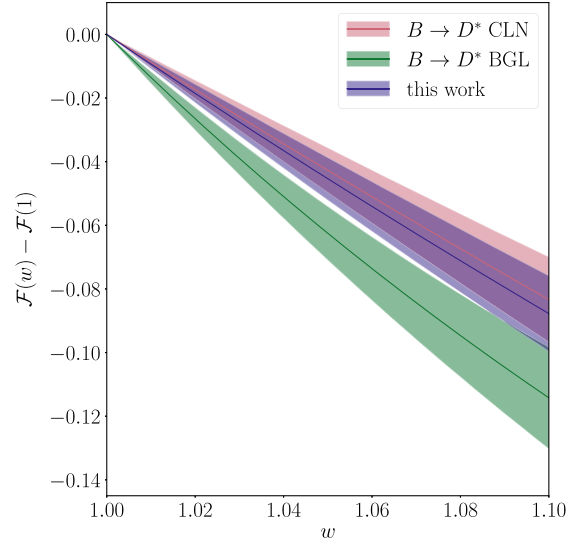


FIG. 16. Plot showing $\mathcal{F}(w) - \mathcal{F}(1)$, defined in Eq. (61), against w for our $B_s \rightarrow D_s^*$ form factors computed here, together with the corresponding values from fits to experimental results for $B \rightarrow D^*$ including light cone sum rule constraints from Ref. [62]. Here we see that our results for the slope of $\mathcal{F}(w)$ in the $B_s \rightarrow D_s^*$ case, which we expect to be close to the slope for $B \rightarrow D^*$, are consistent with the CLN fit but in tension with the BGL fit at the level of $\approx 2.5\sigma$.

$$\begin{aligned} & \frac{d\Gamma(B_{(s)} \rightarrow D_{(s)}^* \ell \bar{\nu}_\ell)}{dw} \\ &= \frac{G_F^2 |\eta_{\text{EW}} V_{cb}|^2}{48\pi^3} (M_{B_{(s)}} - M_{D_{(s)}^*})^2 M_{D_{(s)}^*}^3 \sqrt{w^2 - 1} (w + 1)^2 \\ & \times \left[1 + \frac{4w}{w + 1} \frac{M_{B_{(s)}}^2 - 2wM_{B_{(s)}}M_{D_{(s)}^*} + M_{D_{(s)}^*}^2}{(M_{B_{(s)}} - M_{D_{(s)}^*})^2} \right] \\ & \times |\mathcal{F}^{B_{(s)} \rightarrow D_{(s)}^*}(w)|^2. \end{aligned} \quad (61)$$

In Ref. [62], it was emphasized that, for determining V_{cb} from $B \rightarrow D^* \ell \bar{\nu}_\ell$ decay, information about the slope of $\mathcal{F}^{B \rightarrow D^*}(w)$ at zero recoil, $d\mathcal{F}^{B \rightarrow D^*}(w)/dw|_{w=1}$, could significantly reduce the uncertainty in $|V_{cb}|$. They consider a hypothetical lattice determination of $d\mathcal{F}^{B \rightarrow D^*}(w)/dw|_{w=1} = -1.44 \pm 0.07$, which results in a $\approx 25\%$ reduction in the uncertainty of V_{cb} determined using the BGL parametrization and also moves the values of V_{cb} determined using both CLN and BGL schemes to within $\approx 0.2\sigma$ of one another.

Here we find a value for the slope of

$$\left. \frac{d\mathcal{F}^{B_s \rightarrow D_s^*}(w)}{dw} \right|_{w=1} = -0.94 \pm 0.15, \quad (62)$$

which we determine using a simple finite difference method. This is consistent with the slope for $B \rightarrow D^*$ determined from the CLN parameters extracted from

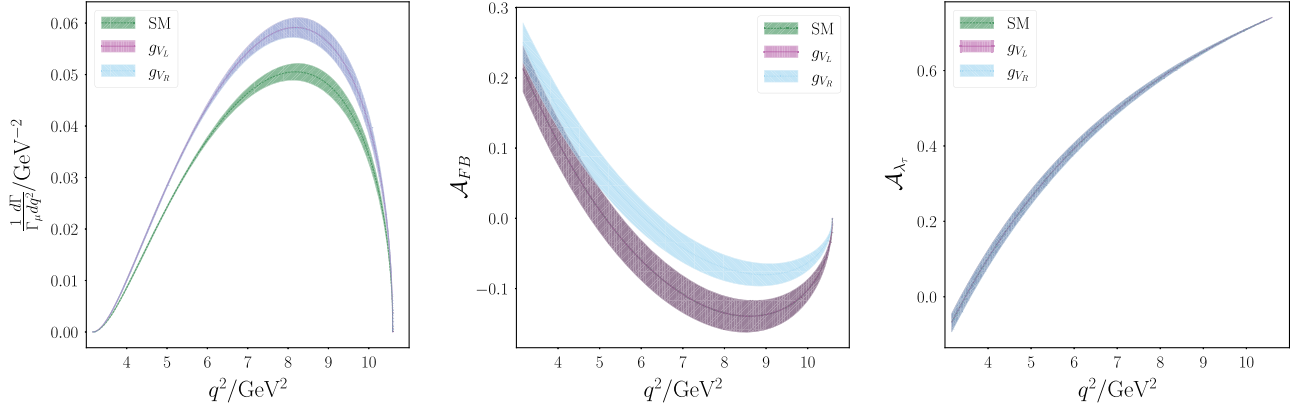


FIG. 17. $d\Gamma/dq^2$, \mathcal{A}_{FB} , and $\mathcal{A}_{\lambda_\tau}$ for $\bar{B}_S^0 \rightarrow D_S^{*+} \tau^- \bar{\nu}_\tau$ in the SM and for the values of g_{V_R} and g_{V_L} given in Eq. (63) from Ref. [10]. $d\Gamma/dq^2$ is normalized to the total rate in the $\ell = \mu$ case, Γ_μ , and the g_{V_L} and g_{V_R} curves overlap. For \mathcal{A}_{FB} , the SM and g_{V_L} curves overlap, and for $\mathcal{A}_{\lambda_\tau}$ all three curves overlap. Note that here we do not include the contribution of δ_{EM} to the uncertainty.

experimental data including light cone sum rule constraints in Ref. [62] of $d\mathcal{F}_{CLN}^{B \rightarrow D^*}(w)/dw|_{w=1} = -0.84(16)$, where we have estimated the uncertainty from the uncertainties of the CLN parameters in Ref. [62], excluding correlations.

In Fig. 16, we have plotted $\mathcal{F}(w) - \mathcal{F}(1)$ against w , where we see the difference between our results for the slope of $\mathcal{F}(w)$ near zero recoil for $B_S \rightarrow D_S^*$ compared to the slope computed from CLN and BGL fits to $B \rightarrow D^*$ experimental data in Ref. [62]. Note that our result for the slope is $\approx 2.5\sigma$ from the slope computed from the BGL fit, which we would expect to be similar for both $B \rightarrow D^*$ and $B_S \rightarrow D_S^*$ based on the small expected size of $SU(3)_{\text{flavor}}$ breaking effects [54].

VII. LFUV OBSERVABLES AND IMPACT OF NEW PHYSICS COUPLINGS

In this section, we study the impact of new physics (NP) couplings on observables in $B_S \rightarrow D_S^*$ decay. We do this by extending the analysis performed in Ref. [19], where the NP couplings extracted from fits to $R(D)$ and $R(D^*)$ in Ref. [10] were used to predict the variations of the relevant observables defined in Ref. [10] away from their Standard Model (SM) values for the case of $B_c \rightarrow J/\psi \ell \bar{\nu}_\ell$. For $B_S \rightarrow D_S^*$, the relevant observables are the same, specifically those defined in Eq. (49) as well as their integrated values and ratios given in Eqs. (50) and (51), respectively, for the SM couplings. We also compute here the value of the tauonic/muonic ratio, $R(D_S^*)$, for different values of new physics couplings. Following Ref. [19], we consider nonzero values for g_{V_R} and g_{V_L} , the complex-valued NP couplings multiplying left- and right-handed NP vector currents additional to those present in the SM. Here, as in Refs. [10,19], we only take these couplings to modify the tauonic decay.

In the left-hand plot of Fig. 17, we plot the tauonic differential rate, normalized by the muonic rate, where we see that both the left- and right-handed NP vector currents

increase the tauonic differential rate markedly. The corresponding values of $R^{g_i}(D_S^*)$ for each NP coupling, together with the numerical values of g_{V_R} and g_{V_L} , are

$$\begin{aligned} g_{V_R} &= -0.01 - i0.39; \\ R^{g_{V_R}}(D_S^*) &= 0.2912(71)_{\text{latt}}(40)_{\text{EM}}, \\ g_{V_L} &= 0.07 - i0.16; \\ R^{g_{V_L}}(D_S^*) &= 0.2915(71)_{\text{latt}}(40)_{\text{EM}}. \end{aligned} \quad (63)$$

These values are both larger than our SM value given in Eq. (44) and are both consistent with the HFLAV average experimental value for $R(D^*) = 0.295(14)$ [1].

The middle and right-hand plots in Fig. 17 show \mathcal{A}_{FB} and $\mathcal{A}_{\lambda_\tau}$, respectively. Here we see that only \mathcal{A}_{FB} , the forward-backward asymmetry of the final-state tau lepton,

TABLE XVI. Integrated angular variables defined in Ref. [10] for the NP couplings given in Eq. (63).

	SM	g_{V_R}	g_{V_L}
$\langle \mathcal{A}_{\lambda_\tau} \rangle$	0.520(12)	0.520(12)	0.520(12)
$\langle F_L^{D_S^*} \rangle$	0.440(16)	0.441(16)	0.440(16)
$\langle \mathcal{A}_{FB} \rangle$	-0.092(24)	-0.033(18)	-0.092(24)

TABLE XVII. LFUV ratios defined in Ref. [10] for the NP couplings given in Eq. (63). Note that as expected from the form of the SM current, a modification to the left-handed vector current does not change any of these ratios away from their SM values.

	SM	g_{V_R}	g_{V_L}
$R(\mathcal{A}_{\lambda_\tau})$	0.524(12)	0.524(12)	0.524(12)
$R(F_L^{J/\psi})$	0.878(18)	0.880(18)	0.878(18)
$R(\mathcal{A}_{FB})$	0.345(56)	0.126(57)	0.345(56)

is sensitive to changes in g_{V_R} only. As expected, modifications to the left-handed current do not result in a change away from the SM. For \mathcal{A}_λ , neither g_{V_R} nor g_{V_L} produce any change. The integrated observables and ratios for these quantities are given in Tables XVI and XVII, respectively, where we repeat the SM results given in Eqs. (50) and (51) for reference. Note that these are all within 1σ of the equivalent quantities computed for $B_c \rightarrow J/\psi \ell \bar{\nu}_\ell$ in Ref. [19].

VIII. CONCLUSIONS

We have extended the heavy-HISQ methods of Ref. [18] to compute the four form factors, $A_0(q^2)$, $A_1(q^2)$, $A_2(q^2)$, and $V(q^2)$, for $B_s \rightarrow D_s^* \ell \bar{\nu}_\ell$ across the full kinematic range of the decay for the first time using lattice QCD. As in Ref. [18], our calculation uses the HISQ action for all quarks, allowing us to normalize the lattice weak current operators that couple the b and c quarks fully nonperturbatively. We have included with this work the complete set of parameters and their correlations needed to reconstruct our form factors, which are expected to be useful in upcoming improved analyses by the LHCb experiment.

Using these form factors, we have presented the first computation in lattice QCD of the total decay rate to each of the three different final-state leptons, as well as the tauonic/muonic ratio. We find [repeating Eqs. (41) to (44)]

$$\begin{aligned} \frac{\Gamma(B_s^0 \rightarrow D_s^{*-} e^+ \nu_e)}{|\eta_{\text{EW}} V_{cb}|^2} &= 2.07(17)_{\text{latt}}(2)_{\text{EM}} \times 10^{13} \text{ s}^{-1}, \\ \frac{\Gamma(B_s^0 \rightarrow D_s^{*-} \mu^+ \nu_\mu)}{|\eta_{\text{EW}} V_{cb}|^2} &= 2.06(16)_{\text{latt}}(2)_{\text{EM}} \times 10^{13} \text{ s}^{-1}, \\ \frac{\Gamma(B_s^0 \rightarrow D_s^{*-} \tau^+ \nu_\tau)}{|\eta_{\text{EW}} V_{cb}|^2} &= 5.14(37)_{\text{latt}}(5)_{\text{EM}} \times 10^{12} \text{ s}^{-1}, \\ R(D_s^*) &= 0.2490(60)_{\text{latt}}(35)_{\text{EM}}, \end{aligned} \quad (64)$$

where the full error budget for these quantities is given in Table XIV. Note that we have included an uncertainty in $R(D_s^*)$ to allow for long-distance QED corrections that could differ between the τ and μ cases. These QED effects must be addressed in future calculations in order to produce results with reliable percent-level uncertainties.

Since the current experimental average for $R(D^*)$ is causing some tension with the SM, we have considered the impact of NP scenarios using our form factors (Sec. VII) and illustrated how a modified left- or right-handed vector current consistent with measurements of $B \rightarrow D^*$ might show up in $B_s \rightarrow D_s^*$ decay. We have shown that these NP currents result in a modified value of $R(D_s^*)$, which is larger than in the SM and is within $\approx 0.6\sigma$ of the current experimental average value of $R(D^*)$.

We have also computed the ratio of total SM rates for $B_s \rightarrow D_s$ and $B_s \rightarrow D_s^*$. We find [repeating Eq. (52)]

$$\frac{\Gamma(B_s^0 \rightarrow D_s^- \mu^+ \nu_\mu)}{\Gamma(B_s^0 \rightarrow D_s^{*-} \mu^+ \nu_\mu)} = 0.443(40)_{\text{latt}}(4)_{\text{EM}}, \quad (65)$$

which is in good agreement with the experimental value from LHCb [6]. We give the forward-backward asymmetry of the final-state lepton, the lepton polarization asymmetry, and the longitudinal polarization fraction in Eq. (50).

We have compared the normalized differential decay rate, $(1/\Gamma)d\Gamma/dq^2$, computed using our form factors, to the recent measurement of the shape of the decay by LHCb. We find that the measurement is broadly consistent with our computed shape, showing only very mild tension which can be seen to originate from a single w bin. We have also used our results to determine the SM CLN parameters ρ^2 , $R_0(1)$, $R_1(1)$, $R_2(1)$, and $h_{A_1}(1)$ for $B_s \rightarrow D_s^*$. The value of the slope of $h_{A_1}(w)$, ρ^2 , measured by LHCb for $B_s \rightarrow D_s^*$ is found to be in good agreement with our computed value, while our values for the other parameters are seen to be consistent with values for the corresponding parameters for $B \rightarrow D^*$.

Finally, we have used our result together with the reconstructed experimentally measured differential decay rate, parametrized using both the CLN and BGL schemes, to compute a value of $|V_{cb}|$. We find that the value computed in this way, using lattice results across the full kinematic range, is consistent with that computed using lattice input for only $h_{A_1}(1)$. Our values for $|V_{cb}|$ computed using experimental results parametrized in the CLN and BGL schemes, respectively, are given in Eqs. (58) and (59). For $|V_{cb}|$, we take the average of their central values, with the larger of the two errors, to find [repeating Eq. (60)]

$$|V_{cb}| = 42.2(1.5)_{\text{latt}}(1.7)_{\text{exp}}(0.4)_{\text{EM}} \times 10^{-3}. \quad (66)$$

This value is not yet accurate enough to resolve the tension between inclusive and exclusive (using $B \rightarrow D^*$ at zero recoil) values for V_{cb} . Note that here, if binned experimental data for the differential rate were available, $|V_{cb}|$ could be determined by comparing our lattice results directly to experiment in a joint fit, without the need to use a parametrization scheme.

Such a model-independent determination of $|V_{cb}|$ using $B_s \rightarrow D_s^*$ would require a reduction in uncertainty by a factor of ≈ 3 in order to be competitive. Such a reduction in the uncertainty of our form factor results is feasible and may be achieved by working on ‘‘exafine’’ lattices with lattice spacings ≈ 0.03 fm, allowing us to work directly at the physical b -quark mass, as well as by including additional configurations to reduce statistical uncertainties at other values of the lattice spacing, as discussed in Sec. V D.

Our work paves the way for the calculation of form factors for $B \rightarrow D^*$ decay across the full range of q^2 . This would also allow a direct determination of $|V_{cb}|$ from unfolded experimental results binned in q^2 , reducing the reliance on extrapolation to the zero recoil point.

ACKNOWLEDGMENTS

We are grateful to the MILC Collaboration for the use of their configurations and code. We thank C. Bouchard, B. Colquhoun, J. Koponen, P. Lepage, E. McLean, and C. McNeile for useful discussions. Computing was done on the Cambridge service for Data Driven Discovery (CSD3), part of which is operated by the University of Cambridge Research Computing on behalf of the DIRAC HPC Facility of the Science and Technology Facilities Council (STFC). The DIRAC component of CSD3 was funded by BEIS capital funding via STFC capital Grants No. ST/P002307/1 and No. ST/R002452/1 and by STFC operations Grant No. ST/R00689X/1. DiRAC is part of the national e-infrastructure. We are grateful to the CSD3 support staff for assistance. Funding for this work came from UK Science and Technology Facilities Council Grants No. ST/L000466/1 and No. ST/P000746/1 and Engineering and Physical Sciences Research Council Project No. EP/W005395/1.

APPENDIX A: LATTICE RESULTS

Here, in Tables XVIII to XXI, we give the lattice results for the form factors, including renormalization factors, which were extracted from the matrix elements in Eq. (13) resulting from the fits discussed in Section III.

APPENDIX B: RECONSTRUCTING THE FIT

Our parametrization of the form factors for $B_S \rightarrow D_S^*$ in the continuum limit is given by Eq. (36). It consists of a pole factor with no uncertainty and a polynomial in z for which the coefficients with their uncertainties are given in

TABLE XVIII. Lattice form factor results for Set 1. ak here is the value of the x and y components of the lattice momentum for the D_S^* . ak is calculated from the corresponding twist in Table IV.

am_h	ak	A_0	A_1	A_2	V
0.65	0.0	...	0.9261(53)
	0.0358913	0.90(13)	0.9251(54)	1.1(2.0)	1.09(48)
	0.0717826	0.898(68)	0.9226(57)	1.21(83)	1.21(22)
	0.107674	0.893(48)	0.9183(61)	1.22(58)	1.23(15)
	0.143565	0.882(38)	0.9120(67)	1.24(50)	1.23(12)
	0.179456	0.867(33)	0.9037(76)	1.26(48)	1.22(10)
0.725	0.0	...	0.9277(54)
	0.0358913	0.92(14)	0.9267(55)	0.8(2.3)	1.10(49)
	0.0717826	0.913(71)	0.9242(58)	1.01(71)	1.22(22)
	0.107674	0.907(50)	0.9199(62)	1.04(42)	1.24(15)
	0.143565	0.897(40)	0.9136(68)	1.06(33)	1.24(12)
	0.179456	0.882(35)	0.9052(78)	1.07(30)	1.23(10)
0.8	0.0	...	0.9299(56)
	0.0358913	0.93(14)	0.9289(57)	0.7(2.7)	1.12(49)
	0.0717826	0.930(75)	0.9264(59)	0.91(76)	1.24(22)
	0.107674	0.924(53)	0.9220(63)	0.95(40)	1.26(16)
	0.143565	0.913(43)	0.9157(70)	0.97(28)	1.25(12)
	0.179456	0.898(37)	0.9073(80)	0.98(23)	1.24(11)

TABLE XIX. Lattice form factor results for Set 2. ak here is the value of the x and y components of the lattice momentum for the D_S^* . ak is calculated from the corresponding twist in Table IV.

am_h	ak	A_0	A_1	A_2	V
0.427	0.0	...	0.908(12)
	0.0524832	0.89(18)	0.906(13)	1.6(1.7)	1.26(56)
	0.104966	0.87(10)	0.896(15)	1.07(96)	1.23(31)
	0.15745	0.824(79)	0.879(18)	0.97(94)	1.19(25)
	0.209933	0.768(75)	0.857(23)	1.0(1.3)	1.13(24)
	0.262416	0.705(78)	0.831(32)	1.2(2.8)	1.06(24)
0.525	0.0	...	0.904(13)
	0.0524832	0.92(20)	0.903(13)	1.9(1.7)	1.26(58)
	0.104966	0.89(11)	0.893(15)	1.13(60)	1.24(33)
	0.15745	0.851(87)	0.875(18)	0.97(46)	1.20(27)
	0.209933	0.792(83)	0.852(24)	0.91(51)	1.14(25)
	0.262416	0.727(86)	0.825(33)	0.90(69)	1.07(26)
0.65	0.0	...	0.900(13)
	0.0524832	0.96(22)	0.898(14)	2.3(2.2)	1.28(61)
	0.104966	0.94(12)	0.888(15)	1.24(63)	1.27(35)
	0.15745	0.891(98)	0.870(19)	1.03(37)	1.22(28)
	0.209933	0.829(93)	0.847(25)	0.94(33)	1.17(27)
	0.262416	0.760(97)	0.821(35)	0.89(37)	1.09(28)
0.8	0.0	...	0.896(14)
	0.0524832	1.02(25)	0.895(14)	2.6(2.8)	1.32(64)
	0.104966	0.99(14)	0.884(16)	1.36(78)	1.31(37)
	0.15745	0.94(11)	0.866(20)	1.10(42)	1.26(30)
	0.209933	0.88(11)	0.843(26)	0.99(31)	1.20(29)
	0.262416	0.80(11)	0.817(36)	0.93(30)	1.13(30)

TABLE XX. Lattice form factor results for Set 3. ak here is the value of the x and y components of the lattice momentum for the D_S^* . ak is calculated from the corresponding twist in Table IV.

am_h	ak	A_0	A_1	A_2	V
0.5	0.0	...	0.8810(73)
	0.0585768	0.963(62)	0.8705(79)	1.00(54)	1.42(19)
	0.117154	0.907(40)	0.839(11)	0.83(18)	1.31(13)
	0.17573	0.818(43)	0.792(18)	0.75(14)	1.20(14)
	0.234307	0.714(59)	0.740(32)	0.66(21)	1.08(18)
	0.292884	0.620(87)	0.676(68)	0.45(45)	0.97(30)
0.65	0.0	...	0.8684(75)
	0.0585768	1.034(73)	0.8584(82)	1.00(74)	1.47(20)
	0.117154	0.976(48)	0.828(11)	0.86(24)	1.36(14)
	0.17573	0.881(51)	0.782(18)	0.79(16)	1.24(14)
	0.234307	0.767(69)	0.731(33)	0.72(17)	1.11(20)
	0.292884	0.66(10)	0.668(70)	0.59(27)	1.00(33)
0.8	0.0	...	0.8580(77)
	0.0585768	1.109(84)	0.8485(84)	0.96(92)	1.54(21)
	0.117154	1.048(55)	0.819(11)	0.88(30)	1.41(14)
	0.17573	0.948(59)	0.774(19)	0.83(20)	1.28(15)
	0.234307	0.823(81)	0.723(33)	0.78(19)	1.15(22)
	0.292884	0.70(12)	0.660(72)	0.67(26)	1.04(36)

TABLE XXI. Lattice form factor results for Set 4. ak here is the value of the x and y components of the lattice momentum for the D_s^* . ak is calculated from the corresponding twist in Table IV.

am_h	ak	A_0	A_1	A_2	V
0.5	0.0	...	0.9244(90)
	0.0356761	0.87(25)	0.9240(92)	8(35)	1.37(93)
	0.0713522	0.88(12)	0.9213(98)	6(25)	1.27(44)
	0.107028	0.874(90)	0.917(11)	20(65)	1.27(33)
	0.142704	0.859(76)	0.911(12)	-7(22)	1.25(27)
	0.178381	0.840(69)	0.904(13)	-1.9(7.4)	1.22(24)
0.65	0.0	...	0.9272(98)
	0.0356761	0.90(29)	0.927(10)	1.7(4.0)	1.4(1.0)
	0.0713522	0.91(14)	0.924(11)	1.2(1.5)	1.28(47)
	0.107028	0.90(10)	0.920(12)	1.2(1.1)	1.28(35)
	0.142704	0.884(88)	0.914(13)	1.14(97)	1.26(29)
	0.178381	0.865(80)	0.906(15)	1.13(97)	1.23(26)
0.8	0.0	...	0.931(10)
	0.0356761	0.93(33)	0.931(11)	1.7(5.6)	1.5(1.1)
	0.0713522	0.95(16)	0.928(12)	1.2(1.6)	1.31(50)
	0.107028	0.94(12)	0.923(13)	1.12(84)	1.31(37)
	0.142704	0.92(10)	0.917(14)	1.07(61)	1.28(30)
	0.178381	0.900(92)	0.909(16)	1.03(53)	1.25(27)

Table XIII. In this section, we give the correlations between the z -expansion coefficients which are necessary for reconstructing our results explicitly, as well as instructions for using the included Supplemental Material [63] to load the z -expansion parameters together with their correlations automatically into PYTHON [64].

The correlation between two coefficients is defined in the usual way as

$$\text{Corr}(X, Y) = \frac{\langle (\bar{X} - X)(\bar{Y} - Y) \rangle}{\sqrt{\sigma^2(X)\sigma^2(Y)}}, \quad (\text{B1})$$

where $\sigma^2(X)$ is the variance of X and \bar{X} is the mean of X . The values are tabulated in Tables XXII–XXXI.

In this calculation and in the Supplemental Material [63], we use the *gvar* PYTHON package to track and propagate correlations. Included in the Supplemental Material [63] are two text files: “CORRELATIONS.txt” contains a dictionary including the means and variances of the z -expansion parameters on the first line and a dictionary detailing the correlations between these parameters on the second line, and “CHECKS.txt” contains arrays of q^2 values and form

TABLE XXII. Correlation matrix for z -expansion coefficients of A_0 .

σ^2	$a_0^{A_0}$	$a_1^{A_0}$	$a_2^{A_0}$	$a_3^{A_0}$
$a_0^{A_0}$	1.0	-0.3781	-0.007023	-0.004275
$a_1^{A_0}$	-0.3781	1.0	-0.1681	0.00345
$a_2^{A_0}$	-0.007023	-0.1681	1.0	-0.002318
$a_3^{A_0}$	-0.004275	0.00345	-0.002318	1.0

TABLE XXIII. Correlation matrix for z -expansion coefficients of A_0 and A_1 .

σ^2	$a_0^{A_1}$	$a_1^{A_1}$	$a_2^{A_1}$	$a_3^{A_1}$
$a_0^{A_0}$	0.2776	-0.02225	0.1044	0.01322
$a_1^{A_0}$	0.04791	0.0006896	-0.2142	-0.02751
$a_2^{A_0}$	-0.01723	0.03742	0.0506	-0.003768
$a_3^{A_0}$	0.003371	-0.008893	0.0279	0.006599

TABLE XXIV. Correlation matrix for z -expansion coefficients of A_0 and A_2 .

σ^2	$a_0^{A_2}$	$a_1^{A_2}$	$a_2^{A_2}$	$a_3^{A_2}$
$a_0^{A_0}$	-0.3816	0.2939	-0.09207	-0.006694
$a_1^{A_0}$	0.03317	-0.4783	0.1869	0.01545
$a_2^{A_0}$	0.1246	-0.2087	-0.01677	0.004254
$a_3^{A_0}$	0.005469	-0.001225	-0.03466	-0.004052

TABLE XXV. Correlation matrix for z -expansion coefficients of A_0 and V .

σ^2	a_0^V	a_1^V	a_2^V	a_3^V
$a_0^{A_0}$	-0.002394	-0.01266	-0.000435	-2.199×10^{-5}
$a_1^{A_0}$	0.003344	0.01268	0.000509	2.598×10^{-5}
$a_2^{A_0}$	-0.001888	0.003397	0.0003099	1.767×10^{-5}
$a_3^{A_0}$	0.0001465	0.0001454	2.376×10^{-5}	1.374×10^{-6}

TABLE XXVI. Correlation matrix for z -expansion coefficients of A_1 .

σ^2	$a_0^{A_1}$	$a_1^{A_1}$	$a_2^{A_1}$	$a_3^{A_1}$
$a_0^{A_1}$	1.0	-0.03043	-0.01583	-0.01588
$a_1^{A_1}$	-0.03043	1.0	-0.3144	0.02958
$a_2^{A_1}$	-0.01583	-0.3144	1.0	-0.09184
$a_3^{A_1}$	-0.01588	0.02958	-0.09184	1.0

TABLE XXVII. Correlation matrix for z -expansion coefficients of A_1 and A_2 .

σ^2	$a_0^{A_2}$	$a_1^{A_2}$	$a_2^{A_2}$	$a_3^{A_2}$
$a_0^{A_1}$	0.3327	-0.09657	0.066	0.01124
$a_1^{A_1}$	0.4326	0.04303	-0.1541	-0.02324
$a_2^{A_1}$	-0.3016	0.5087	0.485	0.05027
$a_3^{A_1}$	-0.005564	-0.007639	0.1149	0.01492

TABLE XXVIII. Correlation matrix for z -expansion coefficients of $A1$ and V .

σ^2	a_0^V	a_1^V	a_2^V	a_3^V
a_0^{A1}	0.008341	0.009546	0.0007997	4.367×10^{-5}
a_1^{A1}	0.01089	0.02048	0.0008922	4.38×10^{-5}
a_2^{A1}	-0.000702	0.01654	0.0008034	4.176×10^{-5}
a_3^{A1}	-0.001079	0.0005229	1.918×10^{-6}	-2.31×10^{-8}

TABLE XXIX. Correlation matrix for z -expansion coefficients of $A2$.

σ^2	a_0^{A2}	a_1^{A2}	a_2^{A2}	a_3^{A2}
a_0^{A2}	1.0	-0.6033	0.1237	-0.001915
a_1^{A2}	-0.6033	1.0	-0.2094	0.01039
a_2^{A2}	0.1237	-0.2094	1.0	-0.07082
a_3^{A2}	-0.001915	0.01039	-0.07082	1.0

TABLE XXX. Correlation matrix for z -expansion coefficients of $A2$ and V .

σ^2	a_0^V	a_1^V	a_2^V	a_3^V
a_0^{A2}	0.01155	-0.025	-0.000755	-3.602×10^{-5}
a_1^{A2}	-0.002784	0.04492	0.001724	8.523×10^{-5}
a_2^{A2}	0.003861	-0.002808	0.0001025	7.013×10^{-6}
a_3^{A2}	0.0008794	4.2×10^{-5}	2.166×10^{-5}	1.227×10^{-6}

TABLE XXXI. Correlation matrix for z -expansion coefficients of V .

σ^2	a_0^V	a_1^V	a_2^V	a_3^V
a_0^V	1.0	-0.4502	0.0155	0.0007512
a_1^V	-0.4502	1.0	-0.1043	-0.003208
a_2^V	0.0155	-0.1043	1.0	-0.0001705
a_3^V	0.0007512	-0.003208	-0.0001705	1.0

factor mean and standard deviation values at the corresponding values of q^2 . This file is used by the PYTHON script *load_fit.py* as a simple check that the fit has been

TABLE XXXII. BGL parameters computed by converting the physical continuum results computed using Eq. (25) to the BGL scheme in Eq. (C2).

	a_0^{BGL}	a_1^{BGL}	a_2^{BGL}	a_3^{BGL}	$\sum (a_n^{\text{BGL}})^2$
F_1	0.002402(90)	-0.0018(44)	-0.041(97)	0.04(82)	0.003(74)
F_2	0.0384(21)	-0.077(45)	-0.25(42)	0.0(1.0)	0.07(21)
f	0.01420(53)	-0.019(14)	-0.0(0.2)	0.0(1.0)	0.00055(84)
g	0.0300(33)	0.0(0.08)	-0.04(54)	0.0(1.0)	0.002(41)

loaded correctly. Running *python load_fit.py* will load the parameters from “CORRELATIONS.txt” and compare values computed at hard coded intervals in q^2 to those in “CHECKS.txt” which were computed as part of this work. Running *python load_fit.py* will also produce some simple plots of the form factors across the full q^2 range. We have tested *load_fit.py* using PYTHON3.7.5 [64], *gvar* 9.2.1 [65], NumPy 1.18.2 [66], and MATPLOTLIB3.1.2 [67].

APPENDIX C: BGL PARAMETERS AND UNITARITY CHECK

1. Conversion to BGL scheme

We may also use our results to determine the parameters entering the BGL parametrization. This allows us to check the unitarity constraints: $\sum (a_n^{\text{BGL}})^2 \leq 1$. To do this, we convert our form factors to the helicity basis, given by Ref. [68]:

$$\begin{aligned}
 g &= \frac{2}{M_{B_s} + M_{D_s^*}} V, \\
 f &= (M_{B_s} + M_{D_s^*}) A_1, \\
 F_1 &= \frac{M_{B_s} + M_{D_s^*}}{M_{D_s^*}} \left[-\frac{2M_{B_s}^2 |\vec{p}'|^2}{(M_{B_s} + M_{D_s^*})^2} A_2 \right. \\
 &\quad \left. - \frac{1}{2} (t - M_{B_s}^2 + M_{D_s^*}^2) A_1 \right], \\
 F_2 &= 2A_0,
 \end{aligned} \tag{C1}$$

where \vec{p}' is the D_s^* spatial momentum in the B_s rest frame. The BGL scheme then parametrizes these form factors using the expansion in z space:

$$F(t) = \frac{1}{P(t)\phi(t, t_0)} \sum_{n=0}^{\infty} a_n^{\text{BGL}} z(t, t_0)^n, \tag{C2}$$

where the pole function P_i is the same as the one we have defined in Eq. (24), and the outer functions ϕ are defined in Ref. [68]. We use the resonance masses given in Ref. [68] in the pole functions P_i . In order to compute the outer functions, we use the values of $\chi_{L(T)}(\pm u)$ computed in Ref. [18]. We use our results to output form factor values in the helicity basis at a large number of q^2 values, which we subsequently fit using Eq. (C2) truncated at $n = 3$. Our

TABLE XXXIII. BGL parameters for our results determined using the BGL parametrization for $B \rightarrow D^*$, compared to the BGL parameters extracted from experimental data, lattice results, and light cone sum rules for $B \rightarrow D^*$ in Ref. [62].

BGL fit:	This work, $B_s \rightarrow D_s^*$	$B \rightarrow D^*$ [62]
a_0^f	0.01258(47)	0.01224(18)
a_1^f	-0.008(15)	-0.052(+27, -15)
a_2^f	-0.03(22)	1.0(+0, -5)
$a_1^{F_1}$	0.00009(402)	-0.0070(+54, -52)
$a_2^{F_1}$	-0.066(61)	0.089(+96, -100)
a_0^g	0.0339(37)	0.0289(+57, -37)
a_1^g	0.005(100)	0.08(+8, -22)
a_2^g	-0.005(315)	-1.0(+2.0, -0)
$a_1^{F_2}$	0.0108(50)	...

results, expressed in terms of the BGL parametrization, are given in Table XXXII, together with the unitarity bounds, which we find to be far from saturation.

2. Comparison to $B \rightarrow D^*$ BGL coefficients

As well as checking that the unitarity constraints are satisfied by the BGL parameters for $B_s \rightarrow D_s^*$, it is also useful and interesting to reparametrize our results using the BGL scheme for $B \rightarrow D^*$. This allows us to compare our results to those for $B \rightarrow D^*$, and also allows for our results to be more readily incorporated into analyses which assume $SU(3)_{\text{flav}}$ symmetry.

The BGL coefficients are sensitive to the meson masses through the outer functions and through the definition of $z(q^2, t_0, t_+)$. In order to reparametrize our results using the BGL scheme for $B \rightarrow D^*$, we first convert our results to the helicity basis, using the B_s and D_s^* masses [as in Eq. (C1)], and then fit these to the BGL parametrization for $B \rightarrow D^*$, in which $z(q^2, t_0, t_+)$ and the outer functions are computed using the B and D^* masses. In order to compare with the

BGL coefficients for $B \rightarrow D^*$ determined in Refs. [62,69], we use the masses and values of $\chi_{L(T)}(\pm u)$ given in Tables IV and III of Ref. [69]. References [62,69] both use the same definitions for the outer functions, given in Ref. [38], which we also use here, as well as choosing $t_0 = t_-$. Note that these definitions differ from those used in Sec. I of Appendix C, from Ref. [68], where the t_+ is given by the true pair production threshold in each channel (e.g., the threshold for BD production for the vector channel and the threshold for B^*D production for the axial-vector and pseudoscalar channels), whereas in Ref. [38] and Refs. [62,69] it is taken to be $(M_{D^*} + M_B)^2$ for all channels. Note also that since our results for $B_s \rightarrow D_s^*$ satisfy the kinematical constraint Eq. (33), involving the B_s and D_s^* masses, the equivalent constraint for $B \rightarrow D^*$ will not be satisfied and so must be imposed. We must also impose the constraint $F_1(q_{\text{max}}^2) = (M_B - M_{D^*})f(q_{\text{max}}^2)$, which will not otherwise be satisfied. We impose these constraints explicitly by using them to fix the zeroth-order coefficients of F_2 and F_1 .

We use a BGL parametrization including up to z^2 terms for f , F_1 , and g , and up to z for F_2 . The coefficients are given in Table XXXIII, where we see that our results are consistent with the BGL parameters for $B \rightarrow D^*$. The correlation matrix for our results in this parametrization scheme is given in Table XXXIV. We conclude that there is no significant effect on the form factors evident in our results with a strange spectator quark compared to those with an up/down one.

APPENDIX D: STABILITY OF OUR FORM FACTORS UNDER VARIATIONS OF THE FIT

1. Variations of correlator fits

In Figs. 18 and 19, we show the variation of the form factors A_0 and A_2 , evaluated at $q^2 = 1 \text{ GeV}^2$, 5 GeV^2 , and 10 GeV^2 , as in Fig. 6. In these plots, we see that these form factors do not change significantly as a result of varying the correlator fit inputs.

TABLE XXXIV. Correlation matrix for our BGL parameters determined using the BGL parametrization for $B \rightarrow D^*$, given in Table XXXIII.

	a_0^f	a_1^f	a_2^f	$a_1^{F_1}$	$a_2^{F_1}$	a_0^g	a_1^g	a_2^g	$a_1^{F_2}$
a_0^f	1.0	-0.097	0.057	-0.192	0.031	0.008	0.011	0.006	0.127
a_1^f		1.0	-0.546	0.191	-0.204	0.014	0.011	-0.043	-0.033
a_2^f			1.0	-0.051	0.007	-0.009	0.024	0.081	-0.059
$a_1^{F_1}$				1.0	-0.737	-0.002	0.036	-0.016	0.177
$a_2^{F_1}$					1.0	-0.001	-0.043	0.019	0.414
a_0^g						1.0	-0.382	0.006	0.002
a_1^g							1.0	-0.087	0.014
a_2^g								1.0	0.007
$a_1^{F_2}$									1.0

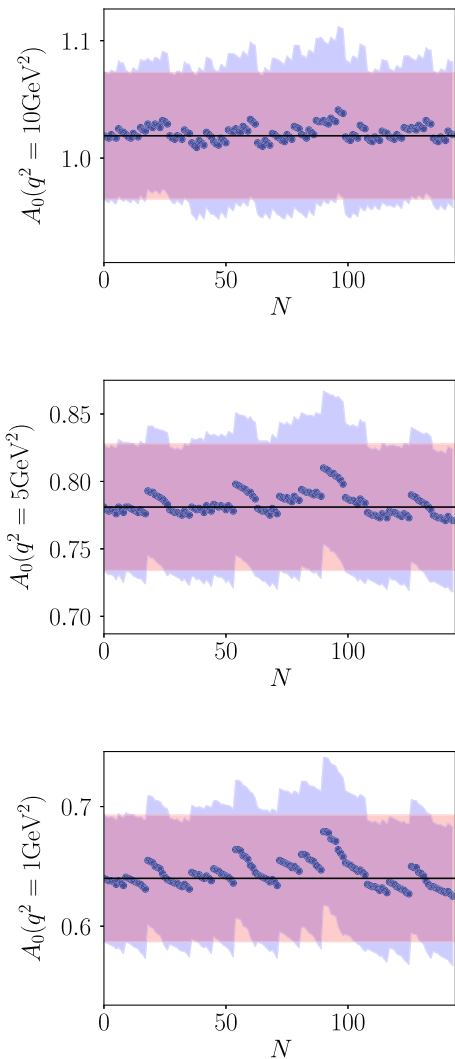


FIG. 18. As for Fig. 6, showing the stability of the form factor A_0 evaluated at $q^2 = 1 \text{ GeV}^2$, 5 GeV^2 , and 10 GeV^2 .

2. Order of expansion

We also investigate the effects of including fewer z terms in Eq. (25) as well as fewer am_c , am_h , and $2\Lambda_{\text{QCD}}/M_{\eta_h}$ terms in Eq. (26). Figure 20 gives the total width, as well as values of the form factors at several values of q^2 , obtained using these variations, where we see that our results are insensitive to the removal of the highest-order terms. We also investigate the effect of increasing or decreasing the prior widths of the parameters b_n^{ijk} in Eq. (26) by a factor of 2. These results are also shown in Fig. 20 where, as in Ref. [18], we see only a very small effect on the central values of our results.

3. Variation of pole term

The pole function in Eq. (24) includes the effects of subthreshold $b\bar{c}$ resonances in q^2 . These begin at the square of the B_c mass, $(6.275 \text{ GeV})^2$, significantly above the

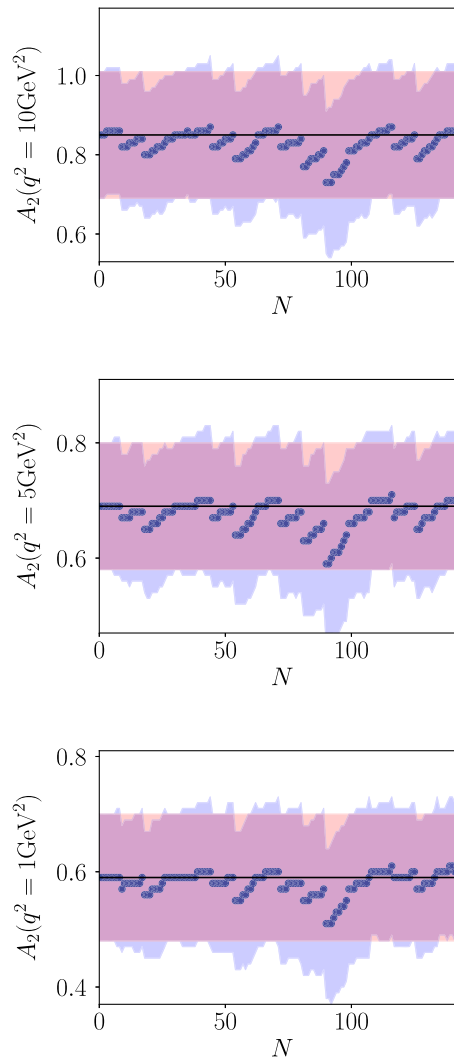


FIG. 19. As for Fig. 6, showing the stability of the form factor A_2 evaluated at $q^2 = 1 \text{ GeV}^2$, 5 GeV^2 , and 10 GeV^2 .

maximum physical value of $q_{\text{max}}^2 \approx (3.25 \text{ GeV})^2$. As such, we do not expect the exact positions or number of poles to have a large effect on the fits, although the choice of the number of poles to include will act as a normalization, changing the magnitude of the coefficients a_n appearing in Eq. (25). Here we investigate the effect of including fewer poles in Eq. (24) by repeating our analysis including only the first N_{poles} resonances listed in Table XII.

We take a prior width on the z -expansion coefficients of $5.0 - N_{\text{poles}}$. We are able to obtain a good fit, with $\chi^2/\text{d.o.f.} \approx 0.1$ in all cases. Since there are only three poles for A_0 expected below t_{+} , we include only three poles for that form factor even in the N_{poles} case.

Figure 21 shows these results, plotting against the left-hand y axis the magnitude of the coefficient corresponding to the order- z term, a_1 , coming from the fits as a function of the number of poles included. Results are given for each form factor. We see that as we include fewer poles,

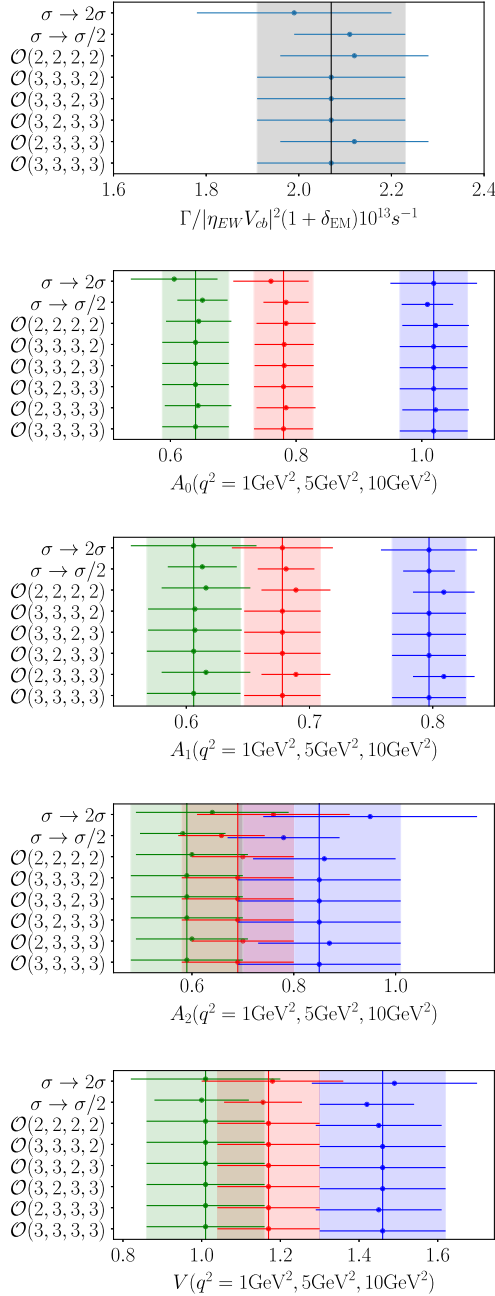


FIG. 20. Plot showing the stability of the total rate for $B_s^0 \rightarrow D_s^{*-} \mu^+ \nu_\mu$, considering lower-order truncations of z -expansion, discretization, and heavy-mass-dependent terms in Eqs. (25) and (26). $\mathcal{O}(n_1, n_2, n_3, n_4)$ corresponds to the result including terms of highest order $\mathcal{O}((2\Lambda/M_{\eta_h})^{n_1}, (am_c)^{2n_2}, (am_h)^{2n_3}, z^{n_4})$. The vertical black line is our final result, corresponding to $\mathcal{O}(3, 3, 3, 3)$, and the gray band is its uncertainty. We also include variations in which we multiply our prior widths by a factor of either 2 or 0.5, labeled as $0(\sigma) \rightarrow 0(\sigma \times 2)$ and $0(\sigma) \rightarrow 0(\sigma/2)$, respectively. Our result for the total rate is very stable to these variations. Note that here we do not include the contribution of δ_{EM} to the uncertainty. We also include similar plots for the form factors, evaluated at $q^2 = 1 \text{ GeV}^2$, 5 GeV^2 , and 10 GeV^2 , plotted in green, red, and blue, respectively.

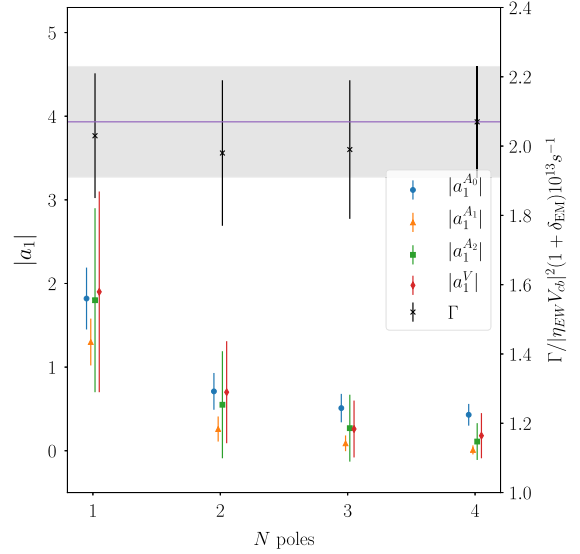


FIG. 21. Magnitude of the $\mathcal{O}(z)$ coefficient, a_1 , for each form factor plotted against the number of poles included in Eq. (24). The prior widths on the b_n^{ijk} are scaled according to the number of poles; see text. Note that the maximum number of poles included for A_0 is 3. The black crosses and error bars give the total width for the $\ell = \mu$ case, $\Gamma/|\eta_{\text{EW}} V_{cb}|^2$, determined from that fit, using the right-hand y axis. The gray band corresponds to our final result for the total width using $N_{\text{poles}} = 4$, and prior values for b_n^{ijk} of 0(1). This shows how the different coefficients as a function of N_{poles} give a very stable result for the total width. Note that here we do not include the contribution of δ_{EM} to the uncertainty in $\Gamma/|\eta V_{cb}|^2$.

increasingly large z -expansion coefficients are needed partly in order to account for the removal of physical q^2 dependence from missing poles, but also because of the normalization change.

4. Inclusion of outer functions

In order to investigate the effect of excluding the outer functions from Eq. (25), we consider using the BGL parametrization described in Sec. I of Appendix C for the extrapolation to the physical point of Sec. IV A. In order to do this, we first convert our lattice data for the form factors to the helicity basis given in Eq. (C1). To evaluate the outer functions ϕ , defined in Ref. [68], as we vary the heavy mass, we must evaluate the function $\chi_{L(T)}(\pm u_h)$, defined in Ref. [38], at different values of u_h . As in Ref. [18], we take $u_b = 0.33$, $m_b^{\text{pole}} = 4.78$, and $\alpha_s = 0.22$. We use $u_h = u_b \times M_{\eta_b}/M_{\eta_h}$ to approximate the heavy mass dependence of u_h , as well as using $m_h^{\text{pole}} = m_b^{\text{pole}} \times M_{\eta_b}/M_{\eta_h^{\text{phys}}}$. Our BGL fit function then has the form

$$F(t) = \frac{1}{P(t)\phi(t, t_0)} \sum_{n=0}^{\infty} a_n^{\text{BGL}} z(t, t_0)^n, \quad (\text{D1})$$

TABLE XXXV. BGL parameters computed using the full BGL scheme, including outer functions, for the physical continuum extrapolation using Eq. (D1). Note that these values are in good agreement with those computed by converting the physical continuum results computed using Eq. (25) to the BGL scheme, given in Table XXXII.

	$a_0^{\text{BGL}'}$	$a_1^{\text{BGL}'}$	$a_2^{\text{BGL}'}$	$a_3^{\text{BGL}'}$	$\sum (a_n^{\text{BGL}'})^2$
F_1	0.00235(10)	-0.0058(63)	-0.04(13)	-0.31(91)	0.10(56)
F_2	0.0357(33)	-0.122(79)	-0.20(87)	0.0(1.0)	0.06(34)
f	0.01388(62)	-0.017(26)	-0.10(54)	0.0(1.0)	0.01(11)
g	0.0329(57)	-0.03(11)	0.01(99)	0.0(1.0)	0.002(21)

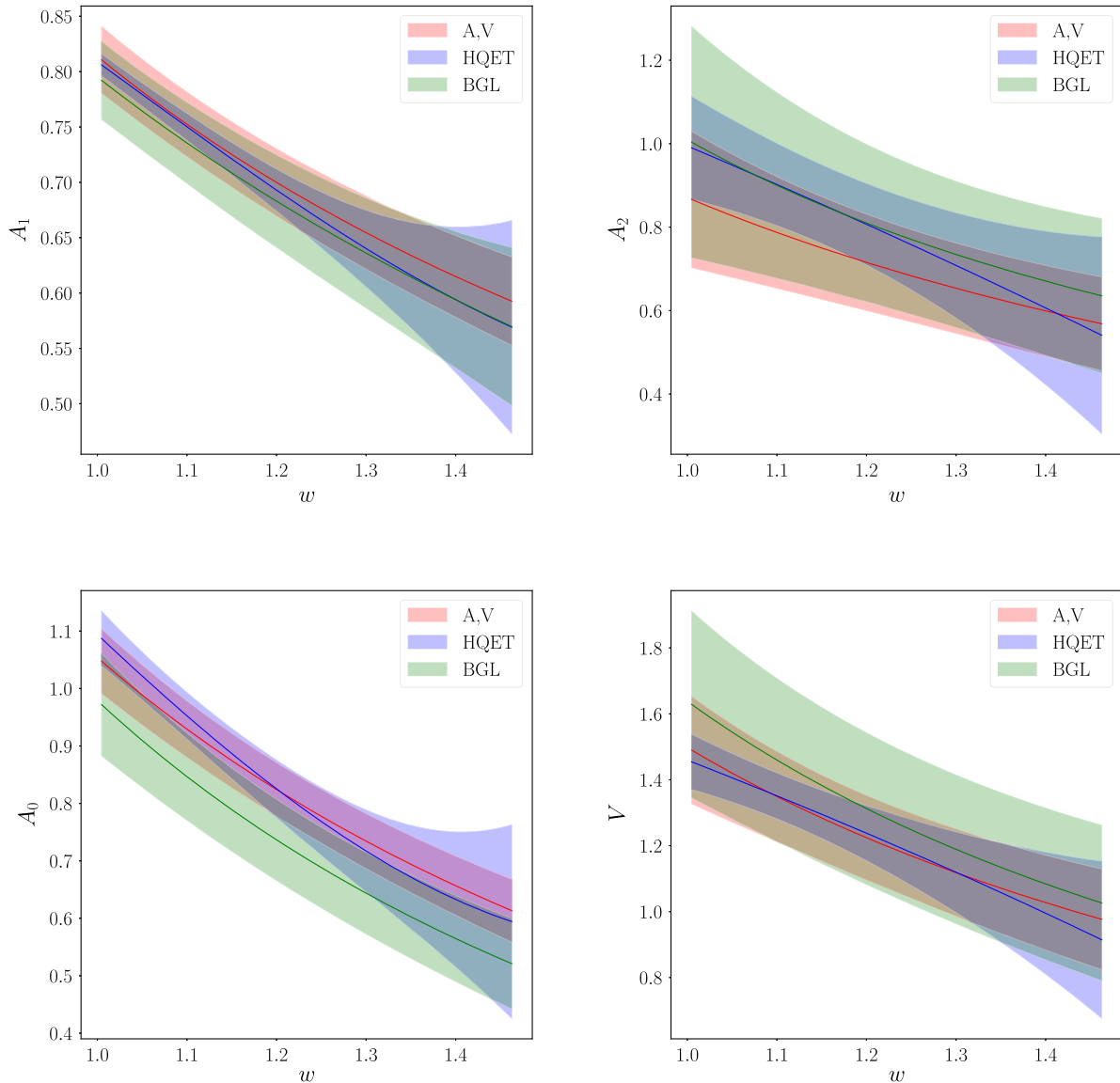


FIG. 22. The form factors as a function of the recoil w . The red curves, denoted “A, V” in the legend, are the result of this work, computed using Eq. (25) to fit the lattice form factor data without the use of outer functions. The green curves use the full BGL parametrization [Eq. (D1)], including the outer functions $\phi(t, t_0)$ and their heavy mass dependence, to fit the lattice form factor data. The blue curves were computed using Eq. (D4), fitting the q^2 dependence using powers of $w - 1$ without including any pole terms or outer functions. Here we see that the three methods produce consistent results for the form factors.

with

$$a_n^{\text{BGL}} = \sum_{j,k,l=0}^3 b_n^{ijkl} \Delta_h^{(j)} \left(\frac{am_c^{\text{val}}}{\pi} \right)^{2k} \left(\frac{am_h^{\text{val}}}{\pi} \right)^{2l} \mathcal{N}_n, \quad (\text{D2})$$

where \mathcal{N} and $\Delta_h^{(j)}$ have the same definitions as in the main analysis discussed in Sec. IV A. We take $t_0 = t_- = q_{\text{max}}^2$ and use the same approximate form as in Sec. IV A for the variation of the pole masses with the heavy quark mass. We take the same priors as in Sec. IV A for the coefficients b_n^{ijkl} and for those entering \mathcal{N}_n . In this fit, we also impose the kinematical constraint at $q^2 = 0$, which here takes the form $2F_1(0) - F_2(0)(M_{B_s}^2 - M_{D_s^*}^2) = 0$. Note that this is equivalent to the constraint $2M_{D_s^*} A_0(0) = (M_{D_s^*} + M_{H_s}) A_1(0) + (M_{D_s^*} - M_{H_s}) A_2(0)$ from the definitions of the helicity basis form factors given in Eq. (C1). We also have, from the definitions in Eq. (C1), the additional condition that $F_1(q_{\text{max}}^2) = (M_{B_s} - M_{D_s^*}) f(q_{\text{max}}^2)$. We impose these conditions both at the physical point and on each lattice, including a nuisance term as in Sec. IV A. Note that here we neglect the running of α_s with heavy mass, allowing for this to be taken up elsewhere in the fit. The results of fitting our lattice data to Eq. (D1) are given in Table XXXV, where we see that the BGL parameters from this fit are very close to those given in Table XXXII, which were computed from the continuum form factors extrapolated to the physical continuum using Eq. (25) without including outer functions. In both cases, the unitarity bounds are far from saturation without the need to impose this constraint in our fits. This shows that the approach adopted here and in Ref. [18], of excluding the outer functions from the physical continuum extrapolation, is consistent with including them.

The physical continuum form factors computed using Eq. (D1) (converted to the A_0, A_1, A_2, V basis) are given in Fig. 22, together with those computed using Eq. (25). The total rate computed using the outer functions is, for the $\ell = \mu$ case, $\Gamma^{\text{BGL}} = 1.88(20)_{\text{latt}}(2)_{\text{EM}} \times 10^{13} \text{ s}^{-1}$, compared to the value $\Gamma = 2.06(16)_{\text{latt}}(2)_{\text{EM}} \times 10^{13} \text{ s}^{-1}$ computed in Sec. V, again demonstrating that the exclusion of the outer functions during the extrapolation to the physical continuum point does not have any significant effect on our results.

In Fig. 22, we also plot form factors resulting from performing the extrapolation in the HQET basis. The form factors in this basis are related to the form factors in the helicity basis by

$$\begin{aligned} g &= \frac{h_V}{M_{B_s} \sqrt{r}}, \\ f &= M_{B_s} \sqrt{r} (1+w) h_{A_1}, \\ F_1 &= M_{B_s}^2 \sqrt{r} (1+w) ((w-r) h_{A_1} - (w-1)(r h_{A_2} + h_{A_3})), \\ F_2 &= \frac{1}{\sqrt{r}} ((1+w) h_{A_1} + (rw-1) h_{A_2} + (r-w) h_{A_3}), \end{aligned} \quad (\text{D3})$$

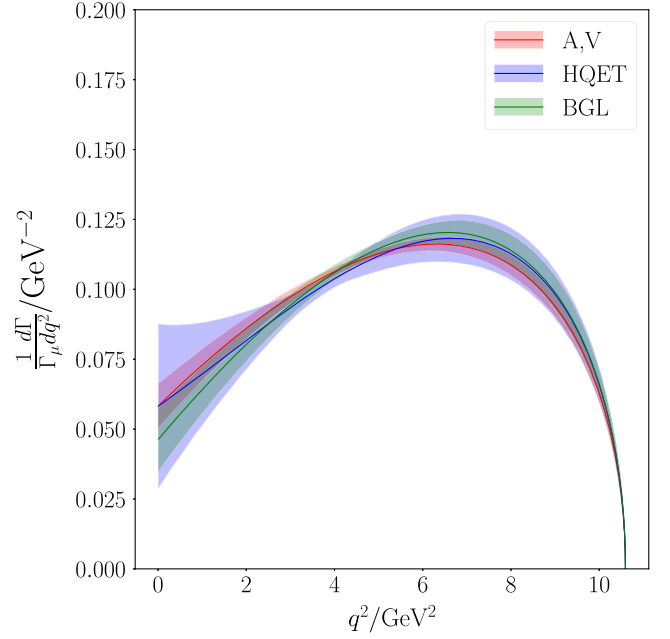


FIG. 23. The normalized differential rate $\frac{1}{\Gamma} \frac{d\Gamma}{dq^2}$ resulting from fit variations. The red curve, denoted “A,V” in the legend, is the result of this work, computed using Eq. (25) to fit the lattice form factor data without the use of outer functions. The green curve uses the full BGL parametrization [Eq. (D1)], including the outer functions $\phi(t, t_0)$ and their heavy mass dependence, to fit the lattice form factor data. The blue curve was computed using Eq. (D4), fitting the q^2 dependence using powers of $w - 1$ without including any pole terms or outer functions. Here we see that the three methods produce consistent results for the differential rate.

and for this extrapolation we use a simple form in powers of $w - 1$, which does not include any information about the pole terms:

$$F(t) = \sum_{n=0}^{\infty} a_n^{\text{HQET}} (w - 1)^n. \quad (\text{D4})$$

Here,

$$a_n^{\text{HQET}} = \sum_{j,k,l=0}^3 b_n^{ijkl} \Delta_h^{(j)} \left(\frac{am_c^{\text{val}}}{\pi} \right)^{2k} \left(\frac{am_h^{\text{val}}}{\pi} \right)^{2l} \mathcal{N}_n. \quad (\text{D5})$$

We see in Fig. 22 that our final results for the continuum form factors, extracted by fitting lattice data to Eq. (25), are broadly consistent with the two alternative fits discussed in this section: the HQET-like fit to simple powers of $w - 1$, Eq. (D4), and the full BGL expression, Eq. (D1). We also show in Fig. 23 that the shape of the differential decay rate resulting from each of these fits is consistent. The total rate for the semimuonic mode resulting from the $w - 1$ fit is $1.95(19) \times 10^{13} \text{ s}^{-1}$, which is consistent with our final result, $\Gamma = 2.06(16)_{\text{latt}}(2)_{\text{EM}} \times 10^{13} \text{ s}^{-1}$, computed using Eq. (25) to perform the extrapolation.

- [1] Y. S. Amhis *et al.* (HFLAV Collaboration), *Eur. Phys. J. C* **81**, 226 (2021).
- [2] J. A. Bailey *et al.* (Fermilab Lattice, MILC Collaborations), *Phys. Rev. D* **89**, 114504 (2014).
- [3] J. Harrison, C. Davies, and M. Wingate (HPQCD Collaboration), *Phys. Rev. D* **97**, 054502 (2018).
- [4] D. Bigi, P. Gambino, and S. Schacht, *Phys. Lett. B* **769**, 441 (2017).
- [5] M. Bordone, M. Jung, and D. van Dyk, *Eur. Phys. J. C* **80**, 74 (2020).
- [6] R. Aaij *et al.* (LHCb Collaboration), *Phys. Rev. D* **101**, 072004 (2020).
- [7] C. Kim, G. Lopez-Castro, S. Tostado, and A. Vicente, *Phys. Rev. D* **95**, 013003 (2017).
- [8] P. Gambino, M. Jung, and S. Schacht, *Phys. Lett. B* **795**, 386 (2019).
- [9] G. Caria *et al.* (Belle Collaboration), *Phys. Rev. Lett.* **124**, 161803 (2020).
- [10] D. Bečirević, M. Fedele, I. Nišandžić, and A. Tayduganov, *arXiv:1907.02257*.
- [11] R. Aaij *et al.* (LHCb Collaboration), *Phys. Rev. Lett.* **120**, 121801 (2018).
- [12] R. Aaij *et al.* (LHCb Collaboration), *arXiv:1808.08865*.
- [13] J. A. Bailey *et al.* (MILC Collaboration), *Phys. Rev. D* **92**, 034506 (2015).
- [14] H. Na, C. M. Bouchard, G. P. Lepage, C. Monahan, and J. Shigemitsu (HPQCD Collaboration), *Phys. Rev. D* **92**, 054510 (2015); **93**, 119906(E) (2016).
- [15] A. Bazavov *et al.* (Fermilab Lattice, MILC Collaborations), *arXiv:2105.14019*.
- [16] E. McLean, C. Davies, J. Koponen, and A. Lytle, *Phys. Rev. D* **101**, 074513 (2020).
- [17] E. McLean, C. T. H. Davies, A. T. Lytle, and J. Koponen, *Phys. Rev. D* **99**, 114512 (2019).
- [18] J. Harrison, C. T. H. Davies, and A. Lytle (HPQCD Collaboration), *Phys. Rev. D* **102**, 094518 (2020).
- [19] J. Harrison, C. T. H. Davies, and A. Lytle (LATTICE-HPQCD Collaboration), *Phys. Rev. Lett.* **125**, 222003 (2020).
- [20] G. C. Donald, C. T. H. Davies, J. Koponen, and G. P. Lepage, *Phys. Rev. Lett.* **112**, 212002 (2014).
- [21] C. McNeile, C. T. H. Davies, E. Follana, K. Hornbostel, and G. P. Lepage (HPQCD Collaboration), *Phys. Rev. D* **85**, 031503 (2012).
- [22] A. Bazavov *et al.*, *Phys. Rev. D* **98**, 074512 (2018).
- [23] D. Hatton, C. T. H. Davies, J. Koponen, G. P. Lepage, and A. T. Lytle, *Phys. Rev. D* **103**, 054512 (2021).
- [24] A. Sirlin, *Nucl. Phys.* **B196**, 83 (1982).
- [25] B. Chakraborty, W. G. Parrott, C. Bouchard, C. T. H. Davies, J. Koponen, and G. P. Lepage, *Phys. Rev. D* **104**, 034505 (2021).
- [26] J. D. Richman and P. R. Burchat, *Rev. Mod. Phys.* **67**, 893 (1995).
- [27] A. Bazavov *et al.* (MILC Collaboration), *Phys. Rev. D* **87**, 054505 (2013).
- [28] A. Bazavov *et al.* (MILC Collaboration), *Phys. Rev. D* **82**, 074501 (2010).
- [29] C. T. Sachrajda and G. Villadoro, *Phys. Lett. B* **609**, 73 (2005).
- [30] D. Guadagnoli, F. Mescia, and S. Simula, *Phys. Rev. D* **73**, 114504 (2006).
- [31] S. Borsanyi *et al.*, *J. High Energy Phys.* **09** (2012) 010.
- [32] R. J. Dowdall, C. T. H. Davies, G. P. Lepage, and C. McNeile, *Phys. Rev. D* **88**, 074504 (2013).
- [33] B. Chakraborty, C. T. H. Davies, P. G. de Oliveira, J. Koponen, G. P. Lepage, and R. S. Van de Water, *Phys. Rev. D* **96**, 034516 (2017).
- [34] B. Chakraborty, C. T. H. Davies, B. Galloway, P. Knecht, J. Koponen, G. C. Donald, R. J. Dowdall, G. P. Lepage, and C. McNeile, *Phys. Rev. D* **91**, 054508 (2015).
- [35] G. C. Donald, C. T. H. Davies, J. Koponen, and G. P. Lepage (HPQCD Collaboration), *Phys. Rev. D* **90**, 074506 (2014).
- [36] G. P. Lepage, corffitter Version 8.0.2, github.com/gplepage/corffitter.
- [37] C. Monahan, J. Shigemitsu, and R. Horgan, *Phys. Rev. D* **87**, 034017 (2013).
- [38] C. Boyd, B. Grinstein, and R. F. Lebed, *Phys. Rev. D* **56**, 6895 (1997).
- [39] I. Caprini, L. Lellouch, and M. Neubert, *Nucl. Phys.* **B530**, 153 (1998).
- [40] R. J. Hill, *eConf C060409* (2006) 027.
- [41] M. Tanabashi *et al.* (Particle Data Group), *Phys. Rev. D* **98**, 030001 (2018).
- [42] R. J. Dowdall, C. T. H. Davies, G. P. Lepage, and C. McNeile, *Phys. Rev. D* **88**, 074504 (2013).
- [43] D. Hatton, C. T. H. Davies, B. Galloway, J. Koponen, G. P. Lepage, and A. T. Lytle (HPQCD Collaboration), *Phys. Rev. D* **102**, 054511 (2020).
- [44] R. Aaij *et al.* (LHCb Collaboration), *Phys. Rev. D* **95**, 032005 (2017).
- [45] A. M. Sirunyan *et al.* (CMS Collaboration), *Phys. Rev. Lett.* **122**, 132001 (2019).
- [46] R. Aaij *et al.* (LHCb Collaboration), *Phys. Rev. Lett.* **122**, 232001 (2019).
- [47] R. J. Dowdall, C. T. H. Davies, T. C. Hammant, and R. R. Horgan, *Phys. Rev. D* **86**, 094510 (2012).
- [48] E. J. Eichten and C. Quigg, *Phys. Rev. D* **49**, 5845 (1994).
- [49] S. Godfrey, *Phys. Rev. D* **70**, 054017 (2004).
- [50] N. Devlani, V. Kher, and A. Rai, *Eur. Phys. J. A* **50**, 154 (2014).
- [51] E. Follana, Q. Mason, C. Davies, K. Hornbostel, G. P. Lepage, J. Shigemitsu, H. Trotter, and K. Wong (HPQCD, UKQCD Collaborations), *Phys. Rev. D* **75**, 054502 (2007).
- [52] P. Zyla *et al.* (Particle Data Group), *Prog. Theor. Exp. Phys.* **2020**, 083C01 (2020).
- [53] L. J. Cooper, C. T. Davies, J. Harrison, J. Komijani, and M. Wingate (HPQCD Collaboration), *Phys. Rev. D* **102**, 014513 (2020).
- [54] M. Bordone, N. Gubernari, D. van Dyk, and M. Jung, *Eur. Phys. J. C* **80**, 347 (2020).
- [55] G. Isidori and O. Sumensari, *Eur. Phys. J. C* **80**, 1078 (2020).
- [56] R. Aaij *et al.* (LHCb Collaboration), *J. High Energy Phys.* **12** (2020) 144.
- [57] C. Oswald *et al.* (Belle Collaboration), *Phys. Rev. D* **92**, 072013 (2015).
- [58] G. P. Lepage, lsqfit Version 11.4, github.com/gplepage/lsqfit.
- [59] C. Bouchard, G. P. Lepage, C. Monahan, H. Na, and J. Shigemitsu, *Phys. Rev. D* **90**, 054506 (2014).

- [60] S. Fajfer, J. F. Kamenik, and I. Nisandzic, *Phys. Rev. D* **85**, 094025 (2012).
- [61] F. U. Bernlochner, Z. Ligeti, M. Papucci, and D. J. Robinson, *Phys. Rev. D* **95**, 115008 (2017); **97**, 059902(E) (2018).
- [62] D. Bigi, P. Gambino, and S. Schacht, *Phys. Lett. B* **769**, 441 (2017).
- [63] See Supplemental Material at <http://link.aps.org/supplemental/10.1103/PhysRevD.105.094506> for loading correlated parameters into PYTHON.
- [64] G. Van Rossum and F. L. Drake, *PYTHON3 Reference Manual* (CreateSpace, Scotts Valley, CA, 2009).
- [65] G. P. Lepage, *gvar* Version 9.2.1, github.com/gplepage/gvar.
- [66] S. van der Walt, S. C. Colbert, and G. Varoquaux, *Comput. Sci. Eng.* **13**, 22 (2011).
- [67] J. D. Hunter, *Comput. Sci. Eng.* **9**, 90 (2007).
- [68] T. D. Cohen, H. Lamm, and R. F. Lebed, *J. High Energy Phys.* **09** (2018) 168.
- [69] D. Bigi, P. Gambino, and S. Schacht, *J. High Energy Phys.* **11** (2017) 061.